REPORT DOCUMENTATION PAGE		Form Approved OMB No. 0704-0188

1. REPORT DATE (DD-MM-YYYY) 28-09-2011	2. REPORT DATE Report Type - Final	3. DATES COVERED (From - To) 08/01/09-06/30/11
4. TITLE AND SUBTITLE Ultralow Loss, Chip-Based Hollow Core Waveguide Using High-Contrast Grating		5a. CONTRACT NUMBER HR0011-09-C-0124
		5b. GRANT NUMBER
		5c. PROGRAM ELEMENT NUMBER
6. AUTHOR(S) Constance Chang-Hasnain		5d. PROJECT NUMBER
		5e. TASK NUMBER
		5f. WORK UNIT NUMBER
7. PERFORMING ORGANIZATION NAME(S) AND ADDRESS(ES) The Regents of the University of California University of California, Berkeley 2150 Shattuck Avenue, Room 313Berkeley, CA 94704-5940		8. PERFORMING ORGANIZATION REPORT NUMBER
9. SPONSORING/MONITORING AGENCY NAME(S) AND ADDRESS(ES) DARPA/CMO Michael Blackstone 3701 N. Fairfax Drive Arlington, VA 22203-1714		10. SPONSOR/MONITOR'S ACRONYM(S)
		11. SPONSORING/MONITORING AGENCY REPORT NUMBER

12. DISTRIBUTION AVAILABILITY STATEMENT
DISTRIBUTION STATEMENT A: UNLIMITED

13. SUPPLEMENTARY NOTES

14. ABSTRACT
The goal of this program is to develop a chip-scale, integrated photonic platform with "fiber-like" losses for optical delay applications. The ability to generate long optical delays with low intrinsic loss is useful for a wide range of high precision military applications and systems including: high time-bandwidth product analog optical signal processors and delay lines for wideband RF systems, optical buffers for all-optical routing networks, and ultra-stable optical interferometers for sensing applications, e.g. rotation sensors. We report a completely new concept of chip-scale hollow-core waveguide (HCW) which eliminates dispersion and nonlinearity in typical waveguide core. We demonstrated a new waveguiding design consisting of two parallel silicon-on-insulator wafers, each containing a single layer of high-contrast subwavelength grating (HCG) to reflect light in-between. The optical confinement without any physical boundary is created by variation of HCG dimensions and demonstrated for the first time in a planar HCW with a record low loss of 0.37 dB/cm. Two-dimensional light confinement in are demonstrated for both straight and curved waveguides. The unique waveguide geometry not only adds new elements into the waveguiding theory, but also will make possible cost-effective manufacturing of integrated optics for chip-scale gas/fluidic sensor, athermal photonic delays lines, and lab-on-a-chip applications.

15. SUBJECT TERMS
Chip-scale, low-loss waveguide, hollow-core waveguide, subwavelength grating

16. SECURITY CLASSIFICATION OF:			17. LIMITATION OF ABSTRACT	18. NUMBER OF PAGES	19a. NAME OF RESPONSIBLE PERSON
			UU	41	Professor Constance Chang-Hasnain
a. REPORT	b. ABSTRACT	c. THIS PAGE			19b. TELEPONE NUMBER (*Include area code*)
U	U	U			510-642-4315

iPhod Project Phase I Report
Title: Ultra-low Loss, Chip-Based Hollow-Core Waveguide Using High-Contrast Grating

PI: Connie Chang-Hasnain, UCB
Co-PI: Ming Wu, Eli Yablonovitch, UCB
Subawards: Alan Willner (USC), and Richard Davis (NGC)
Schedule: Aug. 5, 2009 – Feb. 5, 2011; no cost extension 6/30/2011

Abstract

The goal of this program is to develop a chip-scale, integrated photonic platform with "fiber-like" losses for optical delay applications. The ability to generate long optical delays with low intrinsic loss is useful for a wide range of high precision military applications and systems including: high time-bandwidth product analog optical signal processors and delay lines for wideband RF systems, optical buffers for all-optical routing networks, and ultra-stable optical interferometers for sensing applications, e.g. rotation sensors. We report a completely new concept of chip-scale hollow-core waveguide (HCW) which eliminates dispersion and nonlinearity in typical waveguide core. We demonstrated a new waveguiding design consisting of two parallel silicon-on-insulator wafers, each containing a single layer of high-contrast subwavelength grating (HCG) to reflect light in-between. The optical confinement without any physical boundary is created by variation of HCG dimensions and demonstrated for the first time in a planar HCW with a record low loss of 0.37 dB/cm. Two-dimensional light confinement in are demonstrated for both straight and curved waveguides. The unique waveguide geometry not only adds new elements into the waveguiding theory, but also will make possible cost-effective manufacturing of integrated optics for chip-scale gas/fluidic sensor, athermal photonic delays lines, and lab-on-a-chip applications.

1. Introduction

Hollow-core waveguides show promise for achieving fiber-like performance because of the elimination of the core material. The basic principle is to guide the optical beam propagating through air by multiple reflections at the cladding mirrors. Ultrahigh reflectivity is essential to achieve ultra-low loss hollow waveguides. The UCB approach is to use a novel ultra-low loss hollow-core waveguide structure using high contrast gratings (HCGs) as the high reflectivity cladding to reflect light at a small glancing angle. This concept is illustrated in Fig. 1-1.
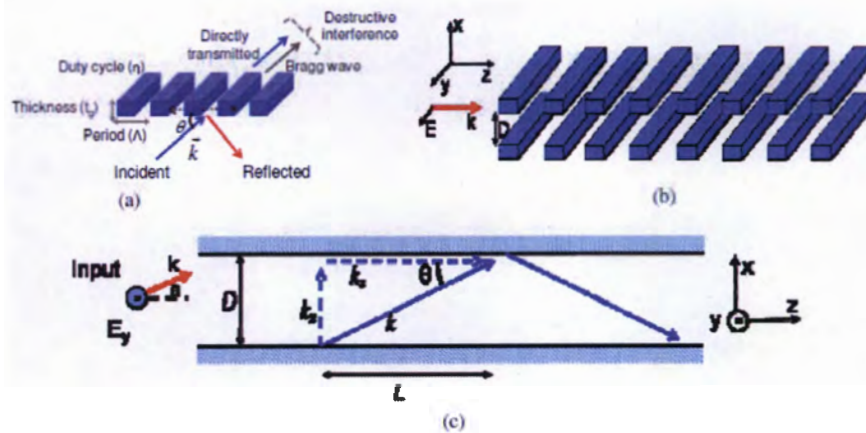
Figure 1-1 | High contrast grating hollow core waveguide. a, Schematic of high contrast grating (HCG). **b,** Schematic of a 1D HCG hollow-core slab waveguide structure. **c,** Ray optics model for guided mode in a hollow-core slab waveguide.

The *Ultra-low loss, chip-based hollow-core waveguide using high-contrast grating* program addresses four critical technical challenges to fully understand and overcome the important loss contributions in integrated optical waveguides.

1. Technical Area One – Ultra-Low-loss Waveguide Design, Fabrication & Testing:

Development of compact, low-loss, polarization-maintaining optical waveguides at telecommunication wavelengths is the primary goal of the program. This includes the development of engineering tools and techniques to assist in the accurate measurement of extremely low on-chip transmission losses.

2. Technical Area Two – High Efficiency Input/Output Coupling & 3D Layer-to-Layer Coupling:

Optimal input/output coupling processes necessary for achieving high transmission throughput is required. Compact delay-based processors demand multi-layer waveguide topologies, which necessitates techniques to achieve efficient layer-to-layer power transfer.

3. Technical Area Three – High Precision On-Chip Optical Splitting/Combining & Trimming:

Both amplitude and phase precision is required for many filtering applications and the ability to accurately set tap weights through optical splitting and combining networks is important. Techniques for trimming and tuning the coupling ratios (amplitude) and delay times (phase) will be demonstrated.

4. Technical Area Four – Optical Delay Application Demonstration:

Scale-up of basic waveguides and devices into a delay-based processor whose performance is commensurate with a realistic military environment.

Overall, the Ultra-low loss, chip-based hollow-core waveguide using high-contrast grating program is a multi-phase program consisting of three development phases with Phase I primarily focusing on Technical Area One; Phase II focusing on Technical Areas One/Two/Three; and

Phase III focusing on Technical Area Four. Table 1 presents a summary of the overall program goals for each of the three phases.

	Phase I	Phase II	Phase III
Waveguide Loss (dB/m)	0.1	0.025	0.01
Time Delay (ns)	100	250	500
Power Handling (mW)	20	50	100
Power-dependent optical phase variation	$\pi/20$	$\pi/20$	$\pi/20$
Footprint (cm^2)	50	20	10
Vertical Layer Coupler Loss (dB)	-	0.5dB	0.2dB
Polarization Extinction Ratio (dB)	-	25 dB	30dB
Split Ratio Precision (50/50)	-	±1%	±0.1%
Time Delay Precision	10^{-2}	10^{-3}	10^{-4}
Optical wavelength	1.55 µm	1.55 µm	1.55 µm
Polarization	Linear	Linear	Linear
Input/output coupler	3dB	0.5dB	0.1dB
Splitter/combiner	±10%	±1%	±0.1%
RF Filtering Bandwidth (GHz)	10	10	10
Number of RF Filtering Taps	4	4	16
Spectral Range (nm)	1	1	10

Table 1. Milestone table for the three phases of the Ultra-low loss, chip-based hollow-core waveguide using high-contrast grating program.

The program focus during Phase I was to develop and demonstrate the overall approach concept with the emphasis on developing and demonstrating the waveguide materials and fabrication techniques required for dramatic transmission loss reduction. The end-of-phase goal was to demonstrate a minimum time delay of 100 ns and assess optical power handling. Also a preliminary design of our candidate Phase III demonstration circuit is provided for Government evaluation.

2. Technical Scope

The goal of the UCB's work is to develop several new Ultra-low Loss Hollow-Core Waveguides Using High-Contrast Gratings on semiconductor wafers and develop high efficiency couplers as well as splitter/combiners for the hollow-core waveguide such that a chip scale optical delay circuit can be realized with a device loss that is order of magnitude lower than the current state-of-the-art in on-chip semiconductor waveguide. More specifically, in Phase I, the goal was to design, fabricate and demonstrate a hollow core waveguide having waveguide loss less than 0.1 dB/m, delay time longer than 100ns, foot print less than 50 square cm and power handling no-less than 20mW.

The scope of the NGAS/USC effort during Phase I encompasses all technical and management activities provided in support of the *Ultra-low loss, chip-based hollow-core waveguide using high-contrast grating* program. Our principal responsibility was the initial design of the demonstration circuit. Our objective was to conduct a design study to determine the

implementation of a delay-based RF signal processor that maximizes the benefits to a selected military mission and to develop conceptual architectures for realizing these benefits. Our effort comprised the three technical tasks described below.

Applications study
- Investigate the principle missions that will benefit from the insertion of iPhoD technology.
- Quantify the required performance characteristics of the iPhoD subsystem.

Architecture study
- Develop a processor architecture that supports the results of applications study.
- Flow down the applications requirements to the specific processor architecture.

Initial processor circuit analysis
- Construct a single-string demonstration model to evaluate the performance limits imposed by the optical components to be used in the Phase III demonstration.
- Quantify compatibility of architecture approaches with HCG waveguide technology.
- Analyze performance metrics for candidate processor architectures.

In the following, the results are discussed in these two major areas: hollow core waveguides and applications.

3. Hollow-Core Waveguides

3.1 Summary of Results

A new class of ultra-low loss hollow-core waveguides (HCWs) is experimentally demonstrated with high-contrast sub-wavelength gratings (HCG) on Si substrate. Light is bounded by two parallel, highly-reflective HCG layers, and propagates in the direction parallel to the grating bars. Optical lateral confinement is achieved by varying the HCG dimensions between the core and cladding region so as to induce different effective indices in the hollow core. *Very low loss, 0.37 dB/cm, is achieved with a ~9 μm waveguide height, the lowest loss measured for an HCW that is mode-matched to a single mode fiber. This is the first experimental realization showing two-dimensional confinement in a low-loss, planar, HCW without side walls.*

A large, 100 μm core, rectangular hollow-core waveguide is demonstrated with HCG as the top and bottom reflectors and distributed Bragg reflector (DBR) as lateral reflectors. *Very low loss <0.1 dB/m is measured. This set up another world record of the lowest loss HCW.* Up to 10 cm long straight waveguides are fabricated and measured with low loss.

The HCG based HCWs establishes an *entirely new scheme* for *cost-effective manufacturing of integrated optics* for chip-scale gas sensors, athermal photonic delay lines, and lab-on-a-chip applications, with the potential to monolithically integrate light sources, detectors and electronics. In particular, the sidewall-free HCWs offer a superb advantage for gas sensing application, as gases can flow instantaneously, not being bounded by the waveguide walls. *The HCG-HCW thus not only stays in line with iPhod program, but also broadens its impact on integrated optics systems.*

4

Curved waveguides are demonstrated. However, the bending loss is significant due to imperfections in HCG dimensions and sidewall roughness, causing excess scattering loss. This limited the bending radius and the total waveguide length integrated on a 6" wafer.

Future project planning includes (1) improved fabrication precision of HCG on wafer scale to result in low loss for curved waveguides with small radius, (2) elimination of wafer warping problem, and (3) demonstration of bonded chips with fixed core size at ~8μm, matched to core size of a single mode fiber. Applications in sensors and low energy all-optical switches based on HCG-HCW would also be explored.

3.2 Low-loss hollow-core waveguide with novel lateral confinement scheme

A hollow-core waveguide (HCW) is best understood by the ray optics model, with an optical beam guided by zig-zag reflections of the guiding walls [1-3]. Thus, the propagation loss is highly dependent on the reflectivity of the walls [1-3] due to a large number of reflections for a given length, $L\lambda/2d^2$ times for length L with core size d at wavelength λ. The lowest losses are 0.2 dB/cm for an HCW with 20 μm core size [2]. However, that particular design does not facilitate fabrication of curved waveguides and efficient single-mode fiber coupling. High contrast grating (HCG) has been discovered to have an extraordinarily broad bandwidth of very high reflection for surface-normal incident light [4-7]. Recently, we proposed and reported numerical simulation results of a one-dimensional (1D) waveguide guided by two HCGs whose periodicity is parallel to the direction of propagation [3].

In the iPhod project, we propose and experimentally demonstrate a completely new class of hollow-core waveguide, schematically shown in Fig. 3-1a. Here, the guided wave propagates along the HCG gratings. The lateral guiding is provided by variation of HCG dimensions to create a lateral effective index, which guides light without physical side walls or boundaries. **Both straight and curved** waveguides are demonstrated using two **parallel, planar wafers**, each containing **one single** layer of HCGs. Such type of two-dimensional (2D) waveguide has never been reported before. This is also the first experimental verification for 2D HCG-HW design using the 1D w-k diagram for HCG-HCW [8] and the effective index method [9] to this new class of hollow core waveguides [3,10]. The propagation loss in a straight waveguide with a ~9 μm waveguide height is measured to be ~0.37 dB/cm. Our result thus represents the lowest loss for an HCW with a small core dimension. The HCG-HCW opens up a new scheme of light guiding for low-loss HCWs, allowing for an entirely new regime of applications.
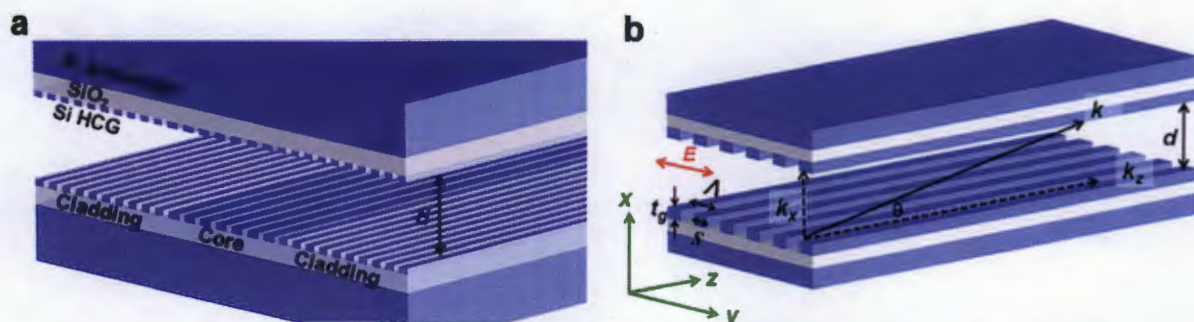

Figure 3-1 | HCG-HCW. a, Schematic of HCG-HCW. The Si HCG sits on top of a SiO₂ layer and Si substrate. The two HCG chips are placed in parallel with a separation gap d, forming an HCW. In the lateral direction, the core and

cladding are defined by different HCG parameters to provide lateral confinement. **b,** Ray optics illustration for a 1D slab HCG-HCW. k vector is decomposed into the propagation constant k_z and transverse component k_x. θ is the angle between k and k_z. d is the waveguide height, and E indicates the oscillation direction of the electrical field. Λ: HCG period; s: Si grating bar width; t_g: HCG thickness.

3.2.a Design

HCGs have been experimentally demonstrated as a high reflection mirrors at normal incident angle for VCSELs [5-7]. An HCG structure consists of a single layer of grating composed of a high-refractive-index material (e.g., Si or III-V compound semiconductor), fully surrounded by a low-index material (e.g., air or oxide). Simulations showed that the high-reflection and wide-bandwidth properties of HCGs also hold true for glancing angles [3]. In addition, HCGs can be designed to reflect incident light with polarization parallel or perpendicular to the grating bars, referred as transverse-electric (TE) and transverse-magnetic (TM) HCG respectively. This work represents the first experimental demonstration of the use of HCG at a glancing angle in a hollow-core waveguide.

Here, the HCGs are fabricated on silicon-on-insulator (SOI) wafers with the gratings formed on the silicon layer above SiO_2. The hollow-core waveguide is formed by placing two HCGs in parallel, separated by a gap d (schematically shown in Fig. 3-1a). In this experiment, we intentionally keep d a variable to better understand and characterize the guiding concept. In the future, monolithically integrated HCG-HWs can be easily manufactured on a wafer-scale by wafer-bonding after grating formation.

In this work, we demonstrate a rather counter-intuitive configuration of hollow-core waveguide with the propagation direction of guided light being parallel to the HCG grating bars. It is easier to understand the gratings as TM-HCGs designed to have high reflection. Note this notation of TM is relative to the gratings and is actually orthogonal to typical definition for waveguide modes.

For 2D waveguiding, it is important to review the 1D design using simple ray optics [3] illustrated in Fig. 3-1b. The propagation loss and the effective index n_{eff} of the fundamental mode are calculated by the following formulae:

$$Loss\ [dB/m] = -10\tan\theta/d_{eff} \cdot \log_{10}|R| \quad (3\text{-}1)$$
$$n_{eff} = \cos\theta = k_z/k \quad (3\text{-}2)$$

where θ is the angle between the ray and the waveguide, k_z is the propagation constant, k is the wave vector of the light in free space, and d_{eff} is the effective waveguide height. d_{eff} takes into account of both the physical waveguide height d and the reflection phase φ_r, which is approximately π in general. The parameter d_{eff} can be calculated by the round trip phase condition of the fundamental mode:

$$2k_x d + 2\varphi_r = 4\pi \quad (3\text{-}3)$$
$$2k_x d + 2\varphi_r = 2k_x d_{eff} + 2\pi \quad (3\text{-}4)$$

For solid-core waveguides, one typical lateral guiding design used was the effective index method [9], utilizing different k_z values in the core and cladding region. Here, we also propose the same - obtaining lateral confinement by different HCG designs for the core and cladding region so that the effective index of the core is higher than that of the cladding. This can be

achieved with the HCG reflection phase, φ_r, which determines the effective index n_{eff} of the 1D-slab waveguide in Eq. (3-2)-(3-4). To insure overall low propagation loss, both HCGs should have high reflectivities. For a fixed HCG thickness t_g, HCG designs with different periods (Λ) and grating widths (s) can provide remarkably large difference of φ_r while maintaining a high reflectivity; this results in a variation in effective index between HCG designs on a flat surface. Also known for solid core waveguides, graded-index typically exhibit lower loss than step-index waveguides [11]. Here, a graded effective-index profile is introduced in hollow-core waveguides with chirped HCG dimensions on the order of tens nanometers.

Figure 3-2 shows the design space of HCG. The propagation loss and the effective index n_{eff} for an HCG hollow-core slab waveguide with 9 µm waveguide height are simulated using rigorous coupled wave analysis (RCWA) [12], for different HCG periods Λ and Si grating bar widths s, with a fixed HCG thickness t_g of 340 nm, and 2 µm buried oxide. The wavelength of the light is 1.55 µm, and the light polarization is TE from the prospective of the waveguide. Based on this design space, we choose the HCG period and Si bar width to be 1210 nm and 775 nm for the core region, and 1060 nm and 635 nm for the cladding region; the HCG parameters in the transition region gradually change from that of the core to the cladding. The relative effective index difference between core and cladding is calculated to be ~0.04%. The core width W_c and the transition region width W_t is designed to be 10.9 µm and 11.9 µm respectively. This design ensures low propagation loss as well as single mode propagation. The cladding width of waveguide is 42.65 µm on each side.
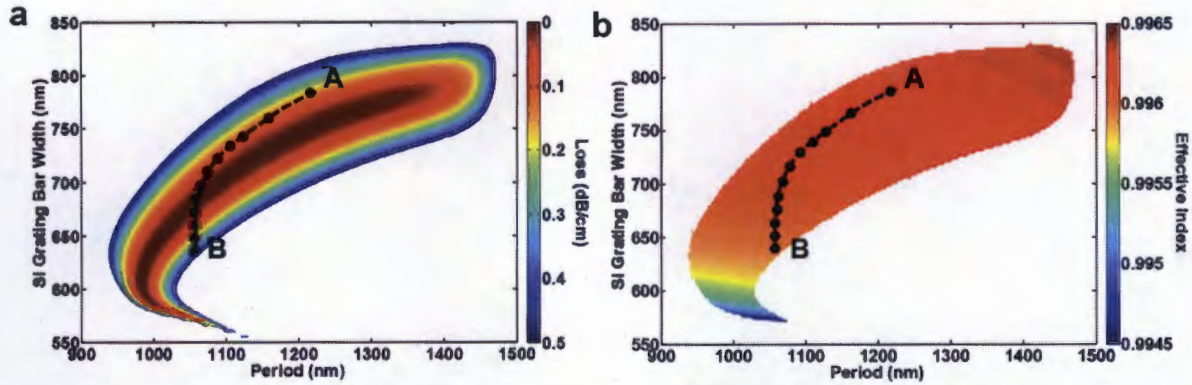

Figure 3-2 | Loss contour plot and effective index contour plot of an HCG hollow-core slab waveguide with a 9 µm waveguide height. The contour plots provide the design space for the waveguide. Different HCG periods Λ and Si grating bar widths s are chosen for the core (point A) and cladding (point B), as well as the transition region (dashed line with dots). The HCG thickness t_g is fixed to be 340 nm, and buried oxide 2 µm. The wavelength of the light is 1.55 µm.

Finite element method (FEM) is used to simulate the mode profile of the fundamental mode of the 2D HCG-HCW, shown in Fig. 3-3a. This results an effective index of 0.9961 and propagation loss of 0.35 dB/cm at 1550 nm. The minimum loss is 0.31 dB/cm at 1535 nm. **It is truly remarkable to note that, although the guided mode has very little energy in the HCGs, a minor parameter change of the HCG on the order of tens nanometers is able to provide phase difference to confine the light laterally.**
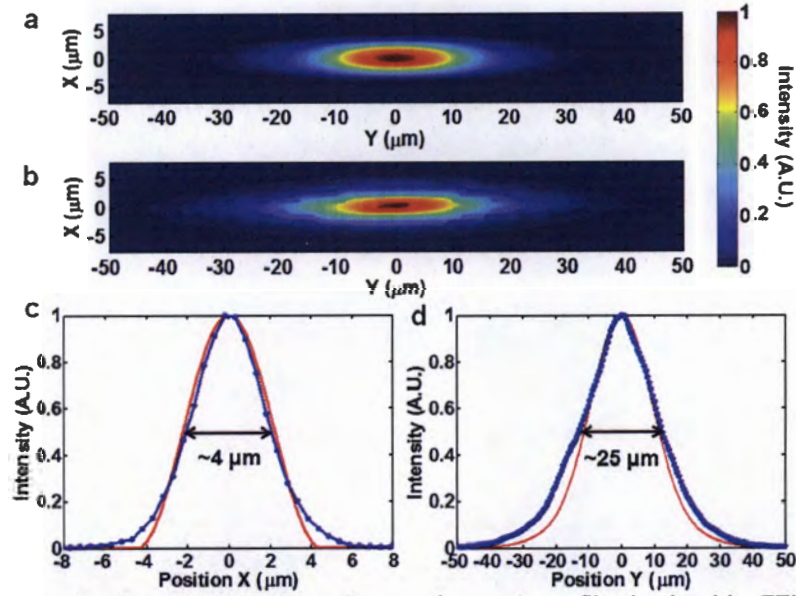
Figure 3-3 | Optical mode of an HCG-HCW. a, Propagation mode profile simulated by FEM. **b,** The measured mode profile from the fabricated device. **c,** Transverse and **d,** lateral mode profile. The simulation (red curve) agrees well with experiment (blue line). The full width at half maximum (FWHM) is 4 μm in the transverse direction, and 25 μm in the lateral direction.

3.2.b Fabrication

The HCG hollow-core waveguide was fabricated using a 6'' SOI wafer. The HCG is patterned with deep ultra-violet (DUV) lithography on the device layer, followed by a standard Si inductively coupled plasma reactive-ion etching (ICP-RIE). With the effective method to obtain lateral guiding, only a single etching step is required. Figure 3-4 shows the top-view optical microscope image of the fabricated chips (a) as well as the SEM image of the core (b) and cladding (c) region HCG of the waveguide. The core, transition, as well as the cladding regions of the waveguide can be clearly distinguished under the optical microscope. The SEM image shows the HCG grating bars, with a smooth surface and sidewall roughness ~10 nm. The HCG dimension is in agreement with the design value, with ~±1.5% variation of the Si grating bar size across the 6'' wafer. This precision is excellent for the DUV used at Berkeley and most of our chips were fabricated with high precision. However, this precision was not easily obtained for longer HCGs, particularly those with bends. It was only realized that, after many months of experimentation, some SOI wafers had rather large warps, which caused imprecision of the HCG dimensions and ultimately contributed to the excess loss. In the future, we will purchase SOI wafers with tighter specifications on warp values.
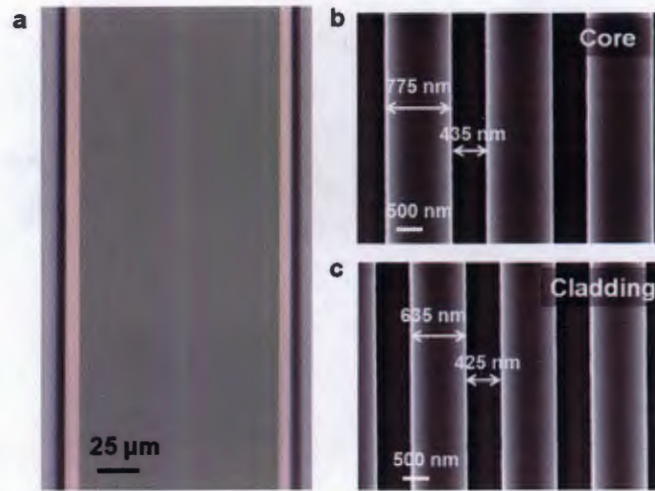
Figure 3-4 | Fabricated HCG hollow-core waveguide chips. a, Optical microscope image of the HCG chip. The core, transition, and the cladding region are clearly distinguished by their diffracted colors. **b,c** The SEM image of the HCG grating bars in the core region and cladding region.

3.2.c Characterization

Waveguides are cut into different lengths for loss measurement. Light is butt-coupled from the waveguide to the photodetector. Figure 3-5 shows the experiment setup. Light guiding in HCG-HCW is experimentally confirmed by launching a laser beam into the waveguide and measuring the intensity profile at the output facet. Figure 3-3b shows the output image with the waveguide height d set to be 9 µm. The measured profiles in the transverse and lateral direction are shown in Fig. 3-3c, d with 4 µm and 25 µm full width at half maximum (FWHM), respectively, at 1550 nm wavelength. Excellent agreement is obtained between simulation and experiment.

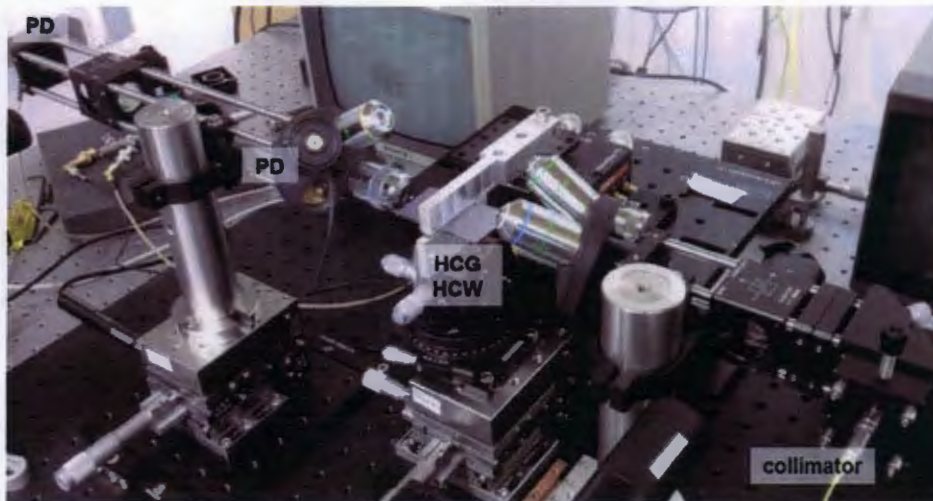**Figure 3-5 | Experimental setup for loss measurement.** The 1.55 µm laser light is first collimated with a collimator, and then launched into the HCW using a 10X objective. A 50X objective is used to collect the light for output facet imaging. For light power detection, a photodetector is placed after the 50X objective and subsequent beam shaping optics; alternatively, the 50X objective can be switched into a photodetector for butt-coupling.

3.2.d Straight waveguide Loss

The net propagation loss and coupling loss are extracted from waveguides with various lengths for d=9 µm waveguides. Figure 3-6a shows the measured total loss spectrum for straight waveguides with 18 mm, 38 mm, 58 mm, and 78 mm length. The extracted propagation loss spectrum agrees well with the simulation results. The minimum loss value from experiment is 0.37 dB/cm at 1535 nm, slightly higher than the simulated value. This difference is attributed to a slight warping of the two HCG chips across their length, which leads to some variation of core height on the order of $<\pm1$ µm. In addition, the HCG surface scattering loss may contribute to additional loss. The coupling loss is estimated to be 4 dB. This can be further reduced with a better matched coupling region.

To better understand the loss of the 2D-confined propagation mode, the loss spectra for the 1D slab HCG-HCW with uniform HCG is simulated by FEM, both for the core and cladding design, shown in Fig. 3-6b. It is seen that the loss spectrum of the 2D-confined propagation mode follows the trend of the 1D slab waveguide. Note that the HCG is optimized for pure 1D TE waveguide mode; with lateral confinement in the 2D case, the propagation mode is no longer pure TE, and this induces additional loss. By further optimizing the HCG dimensions, an even lower loss can be expected.
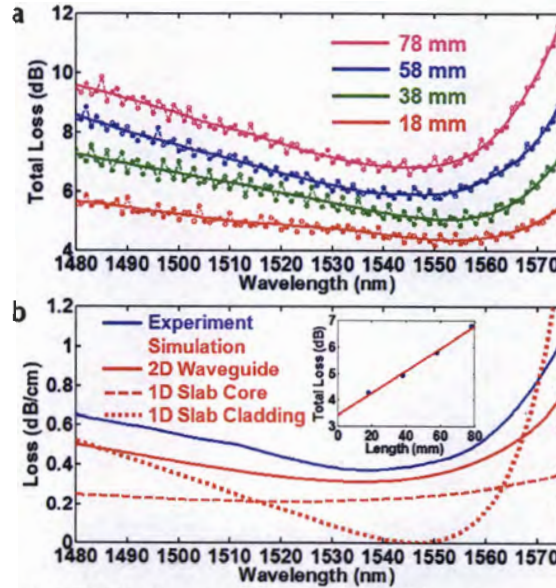

Figure 3-6 | Loss spectrum of HCG hollow-core waveguide with a 9 µm waveguide height. a, Total loss spectrum for an HCG hollow-core waveguide with four different lengths. The dashed dot line is the measured data. The oscillation is due to the laser and a residue FP cavity in the optical path of the measurement system. To remove this noise, a smoothing spline method is applied and the solid curves show the clean spectra. **b,** The extracted propagation loss as a function of wavelength experimentally (blue), and the simulated loss spectrum by FEM (red, solid). The loss spectrum for the slab HCG-HCWs with pure core (red, dashed) or cladding (red, dotted) design are also simulated respectively. Inset: the linear curve fitting to extract the propagation loss and coupling loss at 1535 nm.

3.2.e Control of lateral confinement

The effective index method is the main concept for lateral confinement scheme. This can be further testified and illustrated by varying the waveguide height d. As seen in Fig. 3-1b and Eq. (3-3)(3-4), for a round trip in the transverse direction, the beam acquires phase through two parts: the air trajectory ($2k_x d$), and interaction with HCG ($2\varphi_r$). Between the core and cladding, since the former component is nearly constant, the latter one creates the effective index difference (labeled as $\Delta n/n_{core}$). As d increases, the contribution of $2k_x d$ increases, and thus $\Delta n/n_{core}$ becomes less pronounced. This results in a weaker lateral confinement and a wider spreading of the mode. Fig. 3-7a, b show the experimental measured mode profile and its lateral FWHM versus d respectively. Excellent agreement is obtained with the simulated $\Delta n/n_{core}$ value.

The propagation loss, on the other hand, is not monotonically dependent on d, shown in Fig. 3-7c. This is because the waveguide loss consists of transverse and lateral components. A larger d leads to a weaker lateral confinement, and thus a larger lateral loss. However, the transverse loss decreases since it is proportional to $1/d^2$. Thus there is an optimized d for the lowest loss at a specific wavelength. Figure 3-7c shows the measured loss of the straight waveguide as a function of d. When d is 9 µm, a minimum loss of 0.37 dB/cm is achieved, consistent with that in Fig. 3-6. As d increases up to 10 µm, the lateral loss dominates and total loss increases. The experimental loss agrees with the simulation in general. For larger core height, the discrepancy becomes larger. This is attributed to coupling into higher order modes.

A waveguide with a uniform HCG design and an anti-guided waveguide with the core and cladding design swapped were also fabricated. The output mode profiles are shown in Fig. 3-7d, showing distinct differences with light dispersed in the waveguide without the appropriate HCG design. These demonstrations of lateral confinement prove the effective index method. Here, the effective index method is illustrated, for the first time, for a hollow core waveguide. It is truly remarkable that with little optical energy in HCG, lateral guiding can be obtained with a planar structure. This enables light-guiding in an HCW without the aid of physical side reflectors, and opens up a new regime of optical wave-guiding.
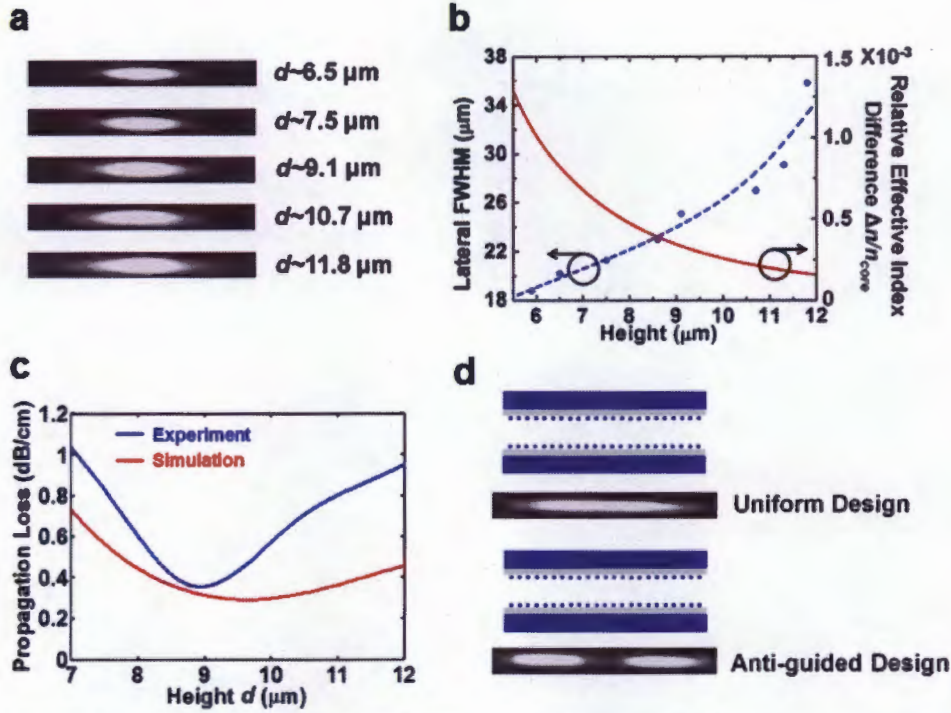
11

Figure 3-7 | Lateral confinement of the HCG-HCW. a, Mode profile at different waveguide heights d. As d increases, $\Delta n/n_{core}$ decreases, and the mode is less confined, suffering increasing lateral leakage. b, Experimental lateral FWHM of the fundamental mode versus different waveguide height d in blue. The blue dashed line curve-fits the experimental sampling points marked with dots. The $\Delta n/n_{core}$ value of the fundamental mode as simulated by FEM is shown in red. The wavelength for the measurement is 1550 nm. c, Propagation loss versus waveguide height d. At the optimized $d\sim9$ um, the best tradeoff between lateral leakage and transverse leakage is achieved. The FEM simulated loss for the first order (i.e. fundamental) and second order transverse mode are also plotted, in reasonable agreement with experiment. d, Mode profile for the hollow-core waveguide with uniform HCG design and anti-guided design where the core and cladding designs are swapped. For each set of mode profiles, the output power of the mode is kept the same, and the image window is 140 μm by 16 μm. The wavelength is set at 1550 nm.

3.2.f Curved waveguide loss

An amazing fact is that light can actually bend and guided by the sidewall-less waveguides. Figure 3-8a and b shows top view of two layouts of the curved waveguide. Various length combinations for Fig. 3-8a is used to extract bending loss. The layout in Fig. 3-8b, on the other hand, demonstrates light guiding by the bend with the output observed in A' rather than B'. The near field intensity profiles for Fig. 3-8a and b configurations are shown in Fig. 3-8c for $d\sim6$ μm, with excellent mode profiles. Figure 3-8d shows loss spectra for various bending radii extracted from the 18 mm and 38 mm waveguides. It is seen that as the bending radius of curvature decreases, the loss spectrum slightly red-shifts. This is because lateral confinement tends to be stronger at longer wavelengths, as indicated by the FEM simulated spectrum of $\Delta n/n_{core}$, shown in Fig. 3-8e. This also explains why the loss difference between the straight and the curved waveguides becomes smaller and smaller as the wavelength increases. In general, the bending loss can be expressed in the following formulae:

$$Loss\ [/cm] = A\exp(\alpha/ROC) \qquad (3\text{-}5)$$
$$Loss\ [dB/cm] = 10\log_{10}A + \frac{10}{ROC}\alpha\log_{10}e \quad (3\text{-}6)$$

12

where ROC is the radius of curvature, and A is a coefficient related to the straight waveguide loss. α indicates how well the light is confined in the curved waveguide, and is strongly correlated with $\Delta n/n_{core}$. For each wavelength, a linear fit is applied to loss versus ROC, and α is extracted. Figure 3-8e shows α versus wavelength: α decreases with increasing wavelength, consistent with the simulated spectrum of $\Delta n/n_{core}$.
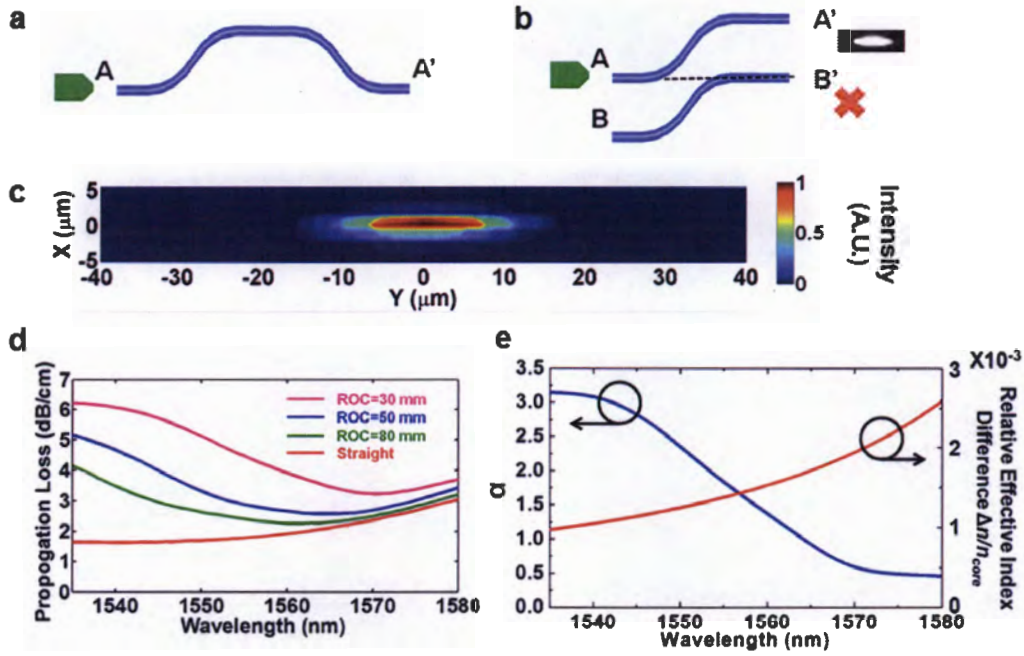

Figure 3-8 | Curving of an HCG hollow-core waveguide. a, **b** Layout of the curved waveguides. Various length combinations of layout **a** is used to extract bending loss. In layout **b**, curved waveguide A-A' and B-B' are in parallel, and the input port of A-A' is aligned with output port of B-B'. Light is launched into port A by a 10X objective. Light guiding by the bend is demonstrated with the output observed in A' rather than B'. **c**, The near field intensity profiles for **a** and **b** configurations with waveguide height $d \sim 6$ μm. **d**, Experimental loss spectrum for waveguides with different radii of curvature ROC. The loss includes both propagation loss and the mode coupling loss at the four bending junctures for a 18 mm chip. **e**, Extracted α versus wavelength, in consistent with the FEM simulated $\Delta n/n_{core}$ spectrum. α is the slope of the linear fit of loss versus ROC^{-1}.

3.3 Large-core hollow-core waveguide

As is mentioned above, a larger core yields a lower transverse mode loss; however the lateral loss would be large due to a weaker confinement. To overcome this problem, distributed Bragg reflector (DBR) is utilized to confine the light laterally. The waveguide structure is schematically shown in Fig. 3-9 with a 100 μm by 100 μm core size. A <0.1 dB/m loss is estimated based on the loss measurement. **This not only reaches the iPhod Phase I loss requirement but also sets up another world record of the lowest loss HCW.**
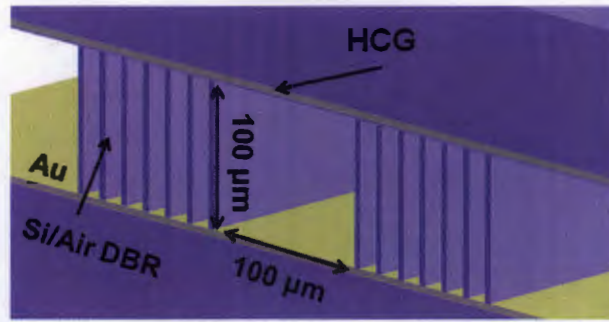
13

Figure 3-9 | Large-core hollow-core waveguide. Light is confined transversely by top HCG layer and bottom Au layer on the SiO$_2$/Si structure, which can also be replaced by HCG through further processing; laterally, light is confined by Si/Air DBR. The core size is 100 μm by 100 μm.

3.3.a Design and fabrication

The DBR is created by a deep etch on an SOI wafer with 100 μm device layer thickness. To overcome the fabrication error during the deep etch, the period as well as the Si thickness of each DBR pair slightly differs from each other. This chirped profile provides a much broader high reflection bandwidth. After the deep etch, Au is subsequently deposited onto the exposed SiO$_2$ layer on the SOI to increase the bottom reflectivity. Another SOI wafer with thin device layer is processed with DUV lithography for the HCG layer. The two SOIs are then placed together to form the waveguide. Figure 3-10 shows the SEM images of the fabricated DBR through Bosh process. The etch profile angle is <0.5°.
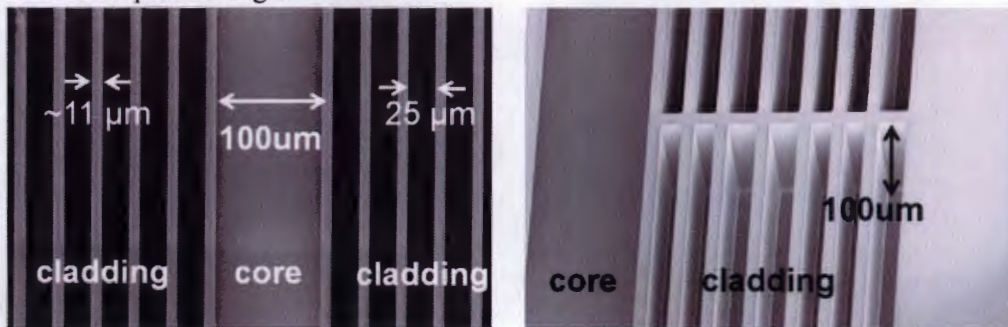

Figure 3-10 | Large-core hollow-core waveguide. The DBR structure is fabricated on an SOI wafer by deep etch Bosh process. Au will be subsequently deposited onto the exposed SiO$_2$ layer. Another SOI wafer is patterned with HCG and would be placed on top of this wafer to form the 100 μm by 100 μm HCW.

3.3.b Characterization

The loss measurement setup is similar to the previous one discussed above, shown in Fig. 3-5. The only difference is that the waist of the launched beam is shaped to be ~35 μm, which is optimized to have a lowest coupling loss ~0.09 dB into the 100 μm by 100 μm HCW. Figure 3-11 shows the loss spectrum of two identical 10 cm long straight waveguides. A minimum loss of ~0.08 dB is achieved at 1563 nm over a 10 cm waveguide including coupling loss. This total loss value is compatible with the 0.09 dB coupling loss, and with the consideration that the measurement uncertainty of the system is ~0.08 dB, it is estimated that the propagation loss of this HCW is <0.1 dB/m. The mode profile of the HCW measured from the experiment matches well with that from the simulation.
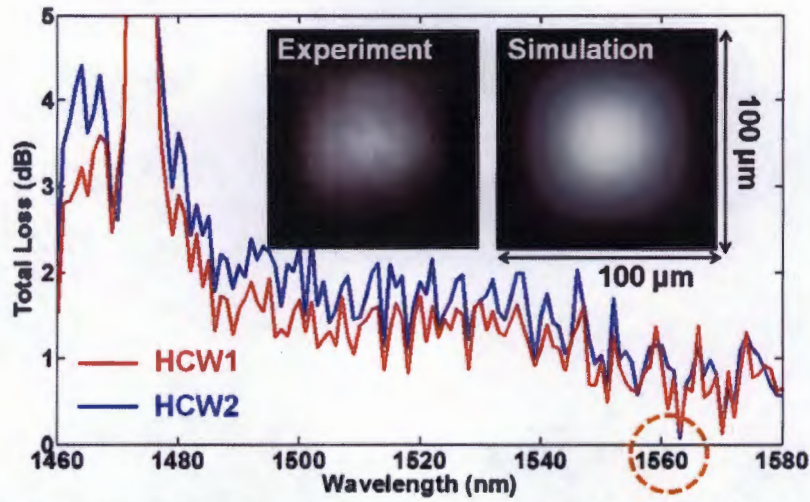
Figure 3-11 | Characterization on large-core HCWs. Total loss spectrum is measured for two identical 100 μm by 100 μm core 10 cm long HCWs. A minimal total loss of ~0.08 dB is obtained at 1563 nm. The experimental mode profile matches well with the simulation.

The waveguide length can be extended by spiral patterns through continuous curving or folded patterns through 45° turning mirror pairs on the 6'' SOI wafer, as shown in Fig. 3-12. The HCG wafer, on the other hand, can be uniform, as its reflectivity is maintained high with different incident directions. The propagation loss is characterized by an optical backscatter reflectometer (OBR). Figure 3-13 shows the measurement results on an HCW with 45° turning mirror pairs. Although the propagation loss for the straight waveguide is very low, it increases dramatically after the first turning. This is due to the fundamental mode scattering into high order modes after the turning, and high order modes have much higher loss. To reduce this loss, a DBR structure with full photonic bandgap for all incident angles is needed. This insures low loss on high order modes. Si/SiO₂ DBR structure can fulfill this requirement [13].
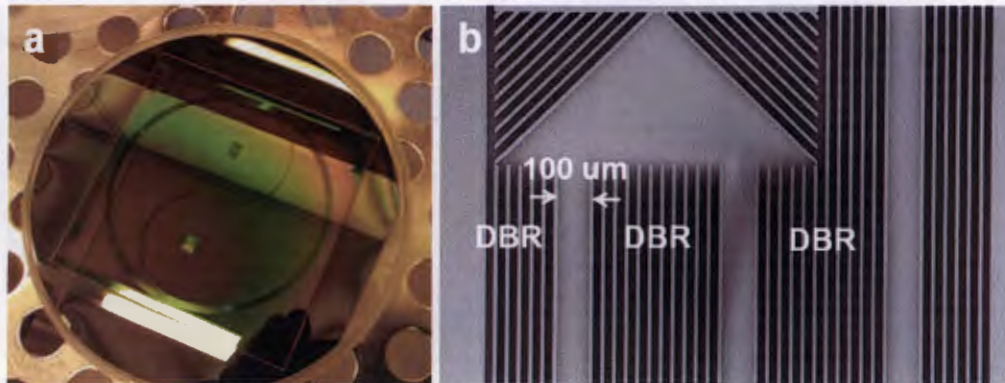

Figure 3-12 | Long HCWs. a, Image of an HCW with spiral pattern through continuous curving. The total length is 1.34 m, with >40 mm radius of curvature in the outer rings and 21.6 mm in the handoff region. Au is deposited on the bottom of the exposed SiO₂ to enhance the reflectivity. **b,** SEM image of a 45° turning mirror pair. This folds the straight HCW and thus aggressively extends the length.
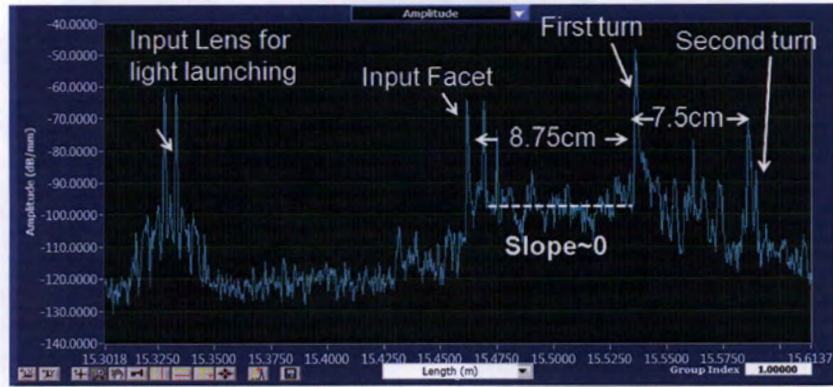
Figure 3-13 | Loss measurement through optical backscatter reflectometer on an HCW. The spikes indicate large reflections, typically because of the interfaces between different optics in the optical path. The slope of the signal indicates propagation loss. The average slope is around zero for the first 8.75 cm straight waveguide, indicating an extremely low loss. After the first turning however, the slope becomes signification, indicating a high loss. This is due to the fundamental mode scattering into high order modes, which have much higher propagation losses. The noise is due to environmental vibration and defects along the waveguide.

3.3.c Nonlinearity measurement

One of the advantages of HCW is its low nonlinearity, as the light propagation media is air. Our nonlinearity measurement is currently limited by maximum power level of our EDFA (~18 dBm), the noise floor of OSA and the insufficient length of the HCW. The upper bound for the nonlinearity coefficient is calculated to be $\gamma=2.3$ /m/W based on our maximum launching power, OSA noise floor and the HCW length. However, we expect it to be much lower in reality because of the hollow core nature.

4. Digital and Analog System Performance in 1D Hollow-core Waveguide

In both electronic and optical systems, time delay is a key basic building block for many applications, such as radio frequency filtering, data traffic engineering, and signal processing. Realizing the delay function in the optical domain might take advantage of its inherent ultrahigh bandwidth and reduce the inefficient optical-electronic conversion. In fiber systems, large optical delays up to several microseconds have been realized using the conversion/dispersion scheme. However, the entire system is relatively bulky and restricts its application. A laudable goal is to make the delay element compact and realize on-chip integration. Nevertheless, most of the on-chip waveguides tend to experience high losses, large dispersions and serious nonlinearity. Thus, it is highly desirable to obtain an on-chip delay element without introducing much signal degradation or distortion. HCW have the potential to achieve all of these features, as light is primarily confined within the air.

A 15-μm core size HW with semiconductor HCGs demonstrates the possibility of realizing an ultra-low loss (0.006 dB/m), small dispersion and negligible nonlinearity, simultaneously [3]. It illustrates the significant possibility of forming an ideal on-chip delay element. We analyze the chromatic dispersion [14] and nonlinearity [15] variation and its effect on high-speed digital and analog signals and systems due to undesired structural parameter changes in 1D Si HCG-HCWs [14-18].

4.1 Dispersion and nonlinearity

In general, chromatic dispersion stems from two sources: material dispersion and waveguide dispersion. As the electric field in the HCG-HCW is highly confined within the air core, the contribution of material dispersion is very limited. Thus, the chromatic dispersion is mainly from waveguide dispersion. We use rigorous coupled wave analysis (RCWA) to calculate the chromatic dispersion of an HCG-HW. The refractive index of silicon is obtained using a build-in Sellmeier equation. Figure 4-1a shows the chromatic dispersion with different HCG-HCW core sizes from 5 to 15 μm. We note that CD is stable around 1.525-μm wavelength, and the third-order dispersion (TOD) or dispersion slope decreases with the core size. This is because the loss is inversely proportional to the square of core size [3]. As the core size decreases, light is confined more tightly and thus experiences more waveguide dispersion. At 1.55-μm wavelength, CD increases to 216 ps/(nm·km) for a 5-μm core size, 25 times larger than the dispersion for a 15-μm core size (8.6 ps/(nm·km)).

Figure 4-1b shows the impact of grating parameters on the nonlinear coefficient of HCG-HCW with different core sizes. As the grating thickness increases or decreases from the optimized parameters, the loss always increases [3]. In such cases, the field confinement provided by the gratings decreases and results in a stronger field-material interaction. Accordingly, the nonlinear coefficient always increases. We should mention that with the increase in the air gap or the decrease in the grating thickness, the total area of nonlinear material (Si) decreases. However, as the significant increase in the interaction between the field and Si gratings is dominant, it always produces a larger γ. Here, we note that for a >200-nm grating parameter variation, γ is still negligibly low (<10-10 /W/m). A similar trend is found for the case of varying the grating period. Moreover, for the HCG-HW with optimized grating parameters, γ decreases three orders of magnitude from 6.54×10^{-10} to 8.15×10^{-13} /W/m as the core size increases from 5 to 15 μm. This is because the loss is inversely proportional to D^2 [3], and the electric field in the grating changes accordingly. Consequently, with the increasing D, the nonlinear coefficient decreases.
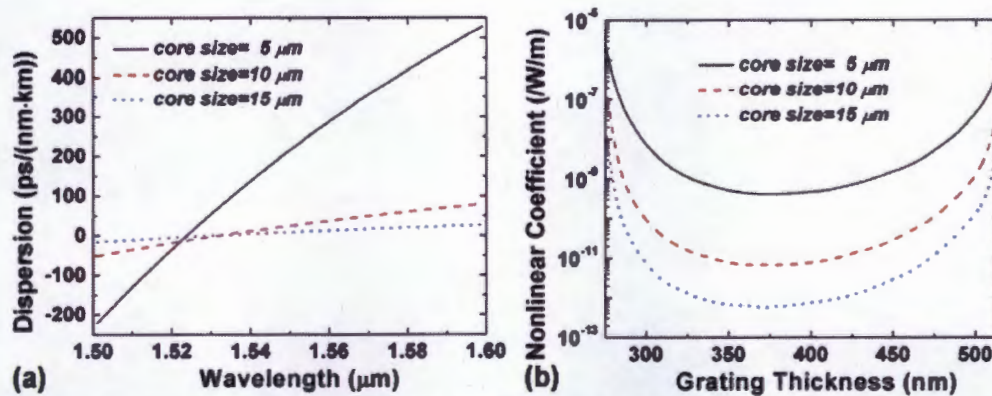

Figure 4-1 | Dispersion and nonlinearity of 1D HCG hollow-core waveguide. a, Dispersion profiles for 1D HCG-HCW (Λ=750 nm, a_g=430 nm, and t_g=340 nm) for core sizes (D) from 5 to 15 μm with a 5-μm step. **b,** Nonlinear coefficient as a function of HCG-HCW grating thickness (t_g) (Λ=750 nm, and a_g=430 nm) for core sizes (D) from 5 to 15 μm with a 5-μm step.

4.2 Digital signal performance

For high-speed signals, the accumulated chromatic dispersion in on-chip waveguides can seriously degrade the transmitted signals. In submicron waveguides, the fabrication tolerance is an important factor that should be taken into account. Figure 4-2a shows the eye opening penalty (EOP) as a function of data rate for different fabrication deviations. We choose 10 mW input power, -10 dBm receiver sensitivity and a 10-m propagation length. Signal is in return-to-zero on-off-keying format (RZ-OOK). The original optimized HCG-HW design has a 5.2×10^{-3} dB/m loss and a 8.6 ps/(nm·km) CD. We used Λ=740 nm, a_g=440 nm, t_g=330 nm for a 10-nm variation, as it has the highest CD of 21.3 ps/(nm·km) in $\pm$10 nm fabrication variation, which is 2.5 times larger than that in the original design. Because of the CD, EOP increases with the bit rate since high data rate signals have a large spectrum bandwidth. The well fabricated HCG-HCW has a penalty below 1 dB for a data rate < 1 Tb/s. Moreover, for 1 Tb/s signals, error-free transmission with bit error rate below 10^{-9} can still be achieved, after 10-m propagation. In contrast, serious signal quality penalty (> 4 dB) is induced for a 640-Gb/s RZ-OOK signal propagating in the 10-m waveguide with 10-nm structural parameter variations. This signal integrity penalty is attributed mainly to the increased CD due to the imperfect fabrication, since induced loss change is independent of signal bit rate.

Long waveguide can provide large delays. For example, a 30-m HCG-HCW will give a 100-ns delay. Figure 4-2b shows the EOP as a function of waveguide length for different fabrication deviations with a 100 Gb/s RZ-OOK signal. The original waveguide supports high-quality signaling over a distance of > 100 m, with an EOP < 1 dB. Loss could increase significantly with fabrication deviation. For a 20-nm structure variation, loss can be as large as 3 dB/m, which causes a large EOP up to 8 dB in a 3-m-long waveguide. The accumulated CD on the waveguide is too low to give noticeable penalty for a 100 Gb/s signal. Since the nonlinearity of HCG-HCW is negligibly low [15], no nonlinearity-induced penalty is observed. This allows us to launch high-power wavelength-division multiplexing (WDM) digital channels into the HCG-HCW with little nonlinear crosstalk.
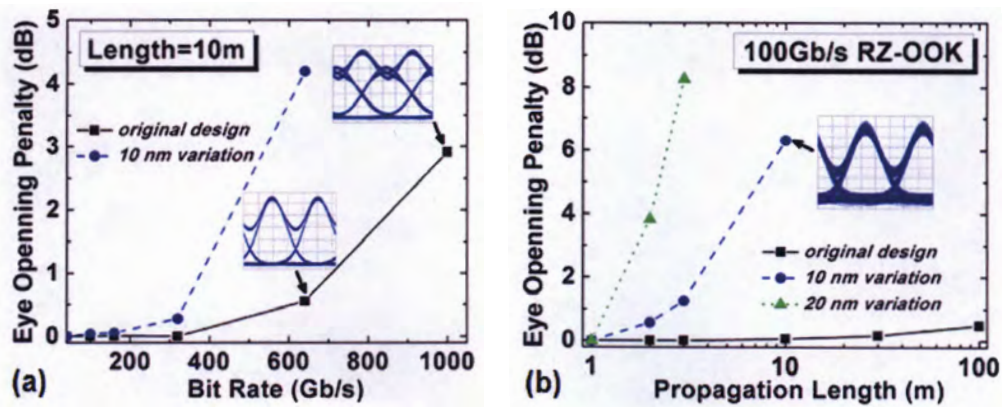

Figure 4-2 | Digital signal performance in 1D HCG hollow-core waveguide. a, EOP as a function of bit rate in RZ-OOK data format for different fabrication deviations in a 10-m-long HCG-HW. **b,** EOP as a function of HCG-HW length for different fabrication deviations with a 100 Gb/s RZ-OOK.

4.3 Analog signal performance

It has been shown that HCG-HCW could exhibit extremely low nonlinearity under a wide variety of waveguide parameters [15]. However, both loss and chromatic dispersion can vary largely with the variation of waveguide parameters and might affect the operation of an analog link or subsystem. Thus it would be very important to characterize the HCG-HW for their suitability in microwave analog applications. The building block of a considered analysis model is shown in Fig. 4-3. A continuous wave (CW) at 1550 nm is generated by a laser source with a line-width of 1 kHz and a RIN of -165 dB. The output power is assumed to be 20-dBm in this paper. Then it is modulated by analog signals (two sine waves with frequencies of 40 GHz and 41 GHz, respectively) through a MZM. The reason why we chose a modulation frequency of around 40GHz is that the HCG-HW is relative linear and there is no notable distortion for analog signal with a lower frequency. The MZM with a half-wave voltage of 5 V is biased at the quadrature point to use the linear portion of the raised-cosine transfer function. The modulated optical signal is then launched into the HCG-HCW for signal transmission. After optical to electrical conversion by a photo-detector with a responsibility of 0.7 A/W, the output signal is analyzed in terms of harmonic distortions and inter-modulation distortions.
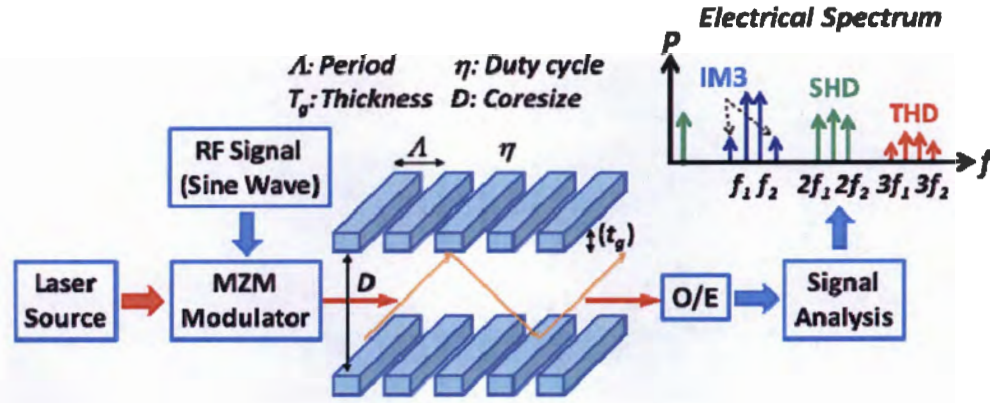

Figure 4-3 | Analysis model of 1D HCG hollow-core waveguide in an analog link.

We obtain the IM3 and SHD SFDRs in a 100-m-long HCG-HW link under the optimal waveguide design. They are 109.9 dB/Hz$^{2/3}$ and 105.7 dB/Hz$^{1/2}$, respectively, at a modulation frequency of 40 GHz, as shown in Fig. 4-4a. The SFDR as a function of modulation frequency is also calculated. As shown in Fig. 4-4b, IM3 SFDR almost remains a constant of 109.9 dB/Hz$^{2/3}$, while SHD SFDR decreases with the increasing modulation frequency, but is still greater than 90 dB/Hz$^{1/2}$ at 80 GHz. For a waveguide with submicron gratings, the fabrication tolerance is also considered. In Fig. 4-4c, two equal peaks at period of around 690 nm and 750 nm can be found for the IM3 SFDR. Both of these changes are caused by optical loss. The effect of dispersion can be observed from changes in the SHD SFDR, which drops with the air gap and increases with the period. In a more realistic case, all three grating parameters (air gap, period and thickness) may change simultaneously by +/-10nm to +/-20nm. There are eight combinations of the three parameters, among which the worst one (with the smallest SFDR) is taken as the lower bound. We make comparisons between the original design, and the lower bounds of a 10-nm variation and a 20-nm variation by calculating SFDR as a function of transmission distance, as shown in Fig. 4-4d. SMF and a low-loss silicon ridge waveguide are also chosen for comparison. The results show that for a propagating length of less than 1000 m, HCG-HWs with an optimal

19

design perform as well as SMF. With fabrication variations both the IM3 and SHD SFDRs degrade, but even with a 20-nm variation on all three grating parameters, HCG-HWs show a much better performance than a low-loss silicon ridge waveguide.
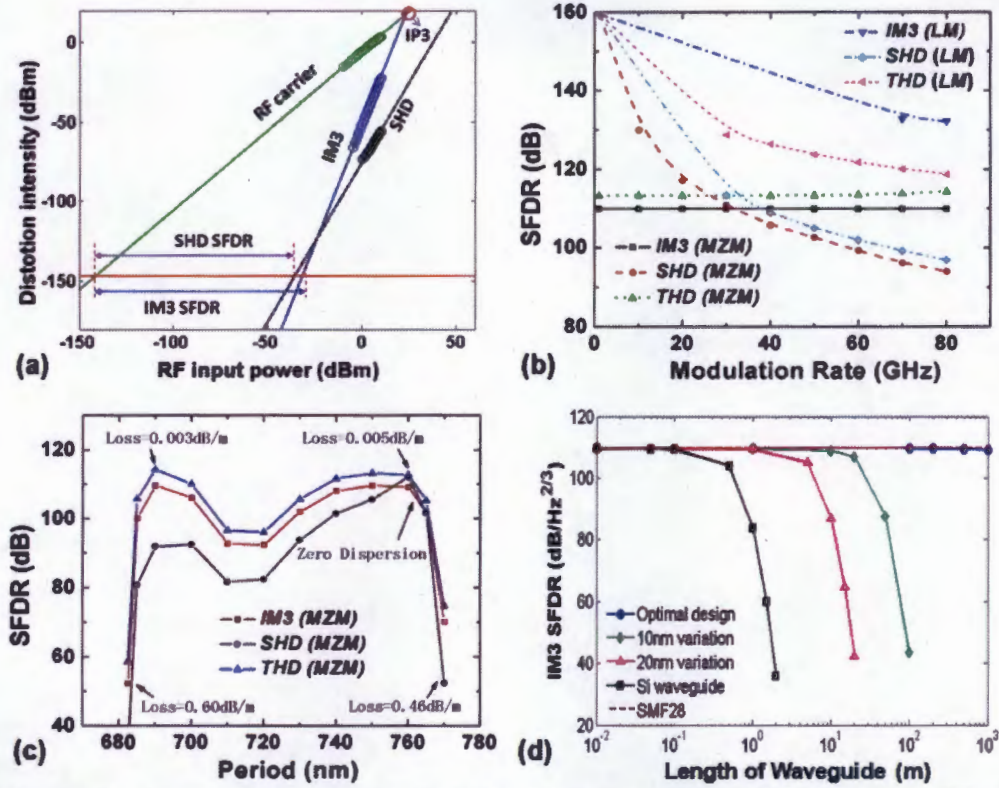

Figure 4-4 | Analog signal performance in 1D HCG hollow-core waveguide. a, Power of RF carrier and distortions as functions of RF input power. **b,** SFDR as function of modulation frequency. **c,** SFDR as a function of grating period. **d,** IM3 SFDR as function of propagating length.

4.4 Application in matched filter

Matched filter is an important element which have been widely used in modern communication and radar systems for its capability of improving signal to noise ratio (SNR) of the upcoming signal degraded by Gaussian noise, and also pulse compression if the input pulse is spectrum spread. Here, we design and evaluate a tapped-delay-line matched filter for a linearly chirped microwave pulse using HCG-HCW. HCG-HW can be potentially built into a multi-taps structure to form a desired Finite impulse response (FIR) matched filter, as shown in Fig. 4-5. An incoherent light source is adopted to avoid beating among different taps. A linear modulator and a linear photo-detector are used to isolate the signal distortions from that induced by HCG-HCW. Based on the classic matched filter (CMF) theory, given an input signal $s(t)$ with $s(\omega)$ as its Fourier Transform, the corresponding matched filter impulse response and frequency response are: $h(t)=s*(-t)$ and $H(\omega)=S*(-\omega)$, respectively. Then the tap weights and delays should be chosen as: $t_k=k\Delta t$ and $a_k=h(t_k)=s*(-t_k)$, respectively. Δt is the delay difference between adjacent taps. Since the widely used spectral-spread (phase modulated or chirped) signal $s(t)$ usually has a complex expression, complex taps are required by CMF theory, which might be difficult to be

realized in optical domain. An all-positive coefficient photonic microwave filter was proposed by using non-uniformly spaced tapped delay line, which is adopted in our design. According to this method, the modified tap weights and tap delays are $\alpha_k'=|\alpha_k|$ and $t_k'=t_k+\varphi(\alpha_k)/2\pi f_0$, respectively, where $\varphi(\alpha_k)$ is the argument of α_k. The tapped delay-line length can be calculated by $L_k = ct_k'/n_{eff}$, where c is the velocity of light, n_{eff} is the effective refractive index of HCG-HCW. Based on the analysis above, a 256-tap FIR matched filter using HCG-HCW is designed and the performances are analyzed. The parameters of the target signal used are as follows: BW=10 GHz, T_0 =4 ns and f_0 =20 GHz.
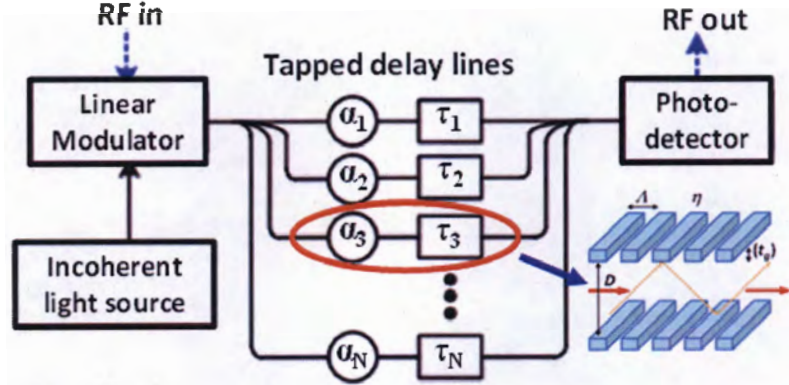

Figure 4-5 | The structure of a microwave photonic tapped delay-line matched filter using HCG-HCW.

SNR gain, Pulse compression ratio (PCR) and Peak to correlation energy ratio (PCE) are the three most important indicators to measure the performance of a matched filter. It has been known that the SNR gain of an input signal can be maximized to twice the TBWP by an idea CMF whose filter frequency response exactly satisfies $H(\omega)=S^*(-\omega)$. Therefore, when we fix the pulse time period and increase the signal BW, the TBWP is linearly increased and so does the SNR gain. Figure 4-6a shows the SNR gain of a matched filter as a function of input signal bandwidth. The red line with circle is the highest SNR gain that can be achieved by an idea matched filter. During the bandwidth range of < 15-GHz, the CMF using HCG-HW has a SNR gain almost comparable to an idea CMF. With further increase of signal bandwidth, the SNR gain does not grow up any more, and even has a trend of decrease when the frequency goes up to 40-GHz.

For the given signal with TBWP of 40 (T_0= 4 ns, BW=10 GHz), the highest SNR gain, PCR and PCE can be achieved with an optimally designed HCG-HW is 18.24-dB, 31.7 and 38.9, respectively, which are 83%, 79.3% and 96.6% of a theoretical value that can be achieved by an idea matched filter. From a perspective of waveguide design, it would be necessary to investigate the dependence of a filter performance on the waveguide structure parameters. The SNR gain as a function of grating period and grating air gap are shown in Fig. 4-6b and c, respectively. The SNR gain is very sensitive to grating period when the core size is 5-μm. A 20-nm variation around optimum value (750-nm) might result in around 8-dB reduction on the SNR gain. This is mainly due to the waveguide loss. However, the filter becomes very stable at 10-μm and 15-μm core size with a more than 70-nm flat-top area. For the air gap, the fabrication tolerance is even larger. The flat-top widths around optimum design (430-nm) are about 90-nm, 120-nm and 150-nm respectively for core size of 5-μm, 10-μm and 15-μm.
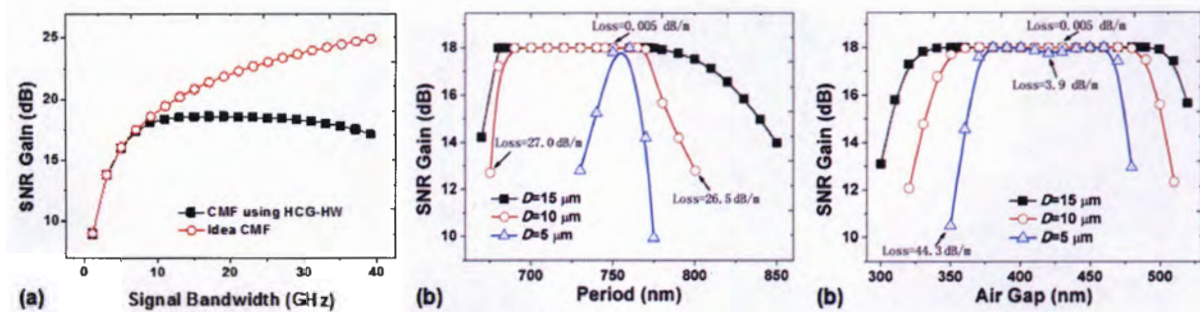
Figure 4-6 | Matched filter performance in 1D HCG hollow-core waveguide. a, SNR gain of designed CMF and an idea CFM as functions of signal bandwidth. **b,** SNR gain of designed matched filter as a function of grating period. **c,** SNR gain of designed matched filter as a function of grating air gap.

5. Applications

5.1 Technical problem

Advancements in MMIC electronics technology have led to the emergence of radars and military communications systems in the modern battlefield environment at frequencies approaching 100 GHz, and with ever increasing bandwidths. The combination of front-end bandwidth, dynamic range, and real-time threat mitigation is a serious challenge to both analog-to-digital converters as well as digital signal processors. This disparity will only widen as advanced MMIC technology continues to cycle into the fielded military systems of traditional and non-traditional foes. Alternatives to conventional digital electronics systems must thus be found to monitor, process, and respond to the threats posed by the modern electronic warfare (EW) environment. Analog techniques avoid the need for high-speed digital conversion and processing, and military systems have employed "frequency-domain" techniques, such as acousto-optic spectrum analyzers, as well as time-domain techniques, such as SAW, MMIC, or coaxial tapped delay lines, for quite some time. These techniques are limited over the bandwidths of interest, however, by nonlinear phase distortion, thermal stability, intra-tap VSWR, nonlinearity, and frequency-dependent loss.

5.2 General methodology

The UCB / NGAS / USC team is addressing this need by exploiting the ability of optical technology to achieve revolutionary advancements in the state of military EW systems. Our critical line of development pursues the advancement of optically-based time-domain techniques, which are a more natural fit than frequency-domain techniques to EW problems such as adaptive filtering of unfriendly jammers, sliding window correlators for matched filtering, and agile waveform generation. A near-term proof-of concept processor in the form of a tapped-delay line processor will be demonstrated by NGAS using extremely low-loss integrated optics waveguide technology incorporated into a novel optical signal combination architecture. This will demonstrate significant advancement relative to existing analog or digital electronic implementations, which are limited in bandwidth, dynamic range, or time-bandwidth product. This delay line approach will provide for rapidly varying, bipolar tap weights and bandwidths exceeding 20 GHz. The need and utility of low-loss waveguides are central to the selection of

this demonstration. Figure 5-1 shows a schematic diagram of our optical processor concept. We feel that this combination of iPhoD technology with COTS components is an ideal vehicle to demonstrate specific iPhoD requirements as delineated in the table of Fig. 5-1.
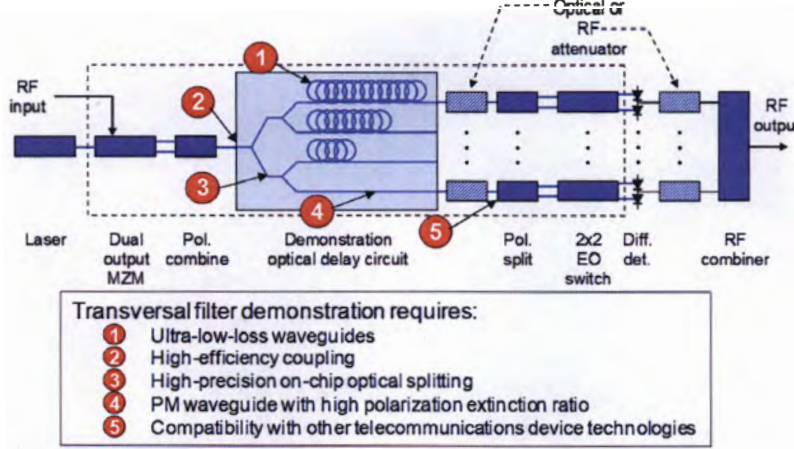

Figure 5-1 | iPhoD demonstration processor.

As the technology matures and higher levels of integration become possible this approach readily can be expanded to compact filters with thousands of taps, which will be necessary to satisfy the requirements discussed in sections 5.3 and 5.4 below. Our overall approach to satisfy the program goals is to perform a system study, then build, and test a demonstration system. Our baseline iPhoD-integrated approach has advantages including:
- Bipolar RF taps
- Delay stability that is not optical wavelength sensitive
- Wideband RF capability
- Incoherent optical summing leads to fabrication tolerances on the order of RF wavelengths not optical wavelengths
- Scalable to filters with thousands of taps
- Parallel optical approach can provide long delays with minimal loss penalty

5.3 Applications study

RF filtering is generally viewed as a frequency selective process, best visualized in the frequency domain, wherein one range of frequencies is passed by the filter while another set of frequencies is rejected. As such, filters are generally characterized by their frequency transfer function, H(f), which is the ratio of the output signal amplitude to the input signal amplitude at frequency f. The response of a filter to an arbitrary input signal, $s_{in}(t)$, is found by decomposing the signal into its frequency components (inverse Fourier transform) then multiplying the signal spectrum by H(f) and reconstructing (Fourier transform) the filtered signal, $s_{out}(t)$. This can also be expressed as a mathematical convolution: $S_{out}(t) = h(t) \otimes S_{in}(t)$, where h($t$) is the filter's impulse response, the discrete-sum approximation of which may be expressed as:

$$s_{out}(t) = \int h(\tau)s_{in}(t-\tau)d\tau \cong \sum_n h(\tau_n)s_{in}(t-\tau_n)$$

This form indicates that any filter response can be implemented by physical processes in the time domain, and can be synthesized (approximately) by summing a discrete set of time-delayed and

23

weighted copies of the input signal. This type of filter, called a transversal filter, was first introduced by Kallman in 1940. A schematic representation of a transversal filter is illustrated in Figure 5-2.
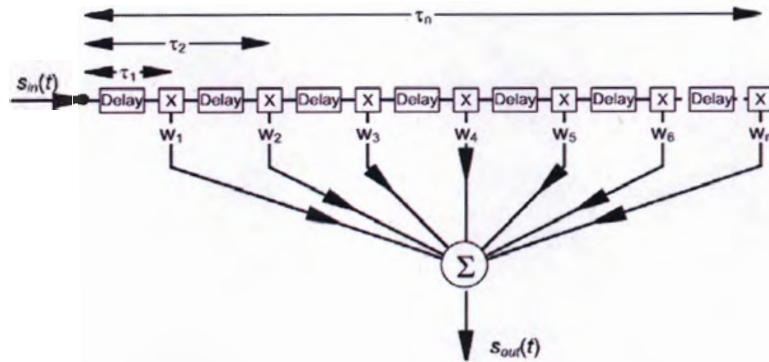

Figure 5-2 | Schematic diagram of a transversal filter.

For many applications it is very desirable to tune the filter by changing the delays and weights. For example, tunable high Q notch filters are useful for nulling spectral interference, reconfigurable matched filters can be used for detecting specific emitters, and arbitrary RF waveforms can be generated by appropriately configuring the filter's impulse response.

Target application
In order to tie the filter requirements to a relevant application we consider the requirements of several future systems that can benefit from the fast and broadband tunable linear phase filter, which can be implemented with the photonic tapped delay line. These filters can be at the front end of a system as in the case of a noise or unwanted signal rejection filter, or at some intermediate point of a system like an IF stage of a tunable receiver. The performance and SWAP (size, weight, and power) requirements of these filters can be very different depending on their location in the system. For phased array systems, front-end filters are associated with every element and as such SWAP performance is key while bandwidth and adjacent channel isolation might usually be secondary. After beam forming, a tunable filter is shared among many elements and SWAP performance is considerably relaxed while high channel-to-channel isolation, narrow pass bandwidth, and sufficient noise rejection is critical. Although some useful general requirements have been obtained, real requirements of systems are based on the specifics of the application and will be used as far as possible to guide the design of the demonstration processor.

The first example of a general filtering requirement is provided by an existing NGAS program specification. Although the entire requirement is provided, the most relevant specifications are indicated with boldface type.

Program Requirement – General Filter
Filter Dimensions   0.4x0.4x1.0   in^3
Frequency   8 - 15 GHz (coverage)
Sub bands   6
Sub band BW   8-10   % (of center frequency)

Insertion Loss   **<1**   **dB**
Return Loss   >16   dB
Pass band Ripple   **< 0.2**   **dB**
Adjacent Band Isolation   **> 60**   **dB (3% from midband)**
Power Handling   4   W (max)
Group Delay   n/a

Since the smallest bandwidth is as great as 640 MHz, the phase across the pass band is easily made linear and a requirement for group delay is not specified. For a photonic implementation the return loss and RF power handling depend only on the input impedance match and can easily be made to meet this requirement since it is straightforward to find a photonic modulator that is very broadband with a good impedance match at the input. Other than the isolation requirement, these requirements are not terribly stringent and should be accommodated with a reasonable number of filter taps.

A second requirement example is that for the filter in a Single-Slice Multi-Mission Unit (SSMMU) being developed by NGAS on a U.S. Government technology contract.

SSMMU Technology Program Requirement – Wideband Filter
Center Frequency   **14.5, 15.5, ..., 19.5**   **GHz**
Passband Width   **1**   **GHz (19.5 GHz channel is 1.1 GHz)**
Insertion Loss   **< 10.5 dB**
Pass band Variation < 2   **dB (equivalent to ripple)**
Loss Variation   **< 4**   **dB (channel to channel)**
Return Loss   >10.9   (equivalent to 1.8:1 ratio)
Adjacent Band Isolation   **> 96 (+IL)**   **dB (± 1.5 GHz from center to DC & 40 GHz)**

SSMMU Technology Program Requirement – Narrowband Filter
Center Frequency   **16, 17, 18, 19** **GHz**
Passband Width   **400**   **kHz**
Insertion Loss   **< 15**   **dB**
Pass band Variation < 2   **dB (equivalent to ripple)**
Loss Variation   **< 4**   **dB (channel to channel)**
Return Loss   >14   (equivalent to 1.5:1 ratio)
Adjacent Band Isolation   **> 96 (+IL)**   **dB (± 1 GHz from center to DC & 40 GHz)**

The format of this specification is similar to the first example and the filters can be designed in a similar manner as well. The adjacent band isolation presented above is a summarized version of the actual requirement. The actual requirement is given for specified bands and frequencies, most likely a consequence of the anticipated filter technology and implementation. For these examples the most stringent requirements have been assumed and are presented to provide a goal for the most aggressive filter design. The pass bandwidths shown above have been assumed to be the – 3 dB bandwidths. The requirement for the narrowband filter specifies 5 dB of rejection ± 5 MHz from the center frequency and 15 dB of rejection ± 10 MHz from the center frequency. In order to meet this requirement, the filter design can be adjusted manually with little effort.

5.4 Architecture study

5.4.1 FIR transversal filter analysis

We have previously performed a preliminary analysis that we present here to demonstrate that the iPhoD technology offers the capability to provide the performance required by military RF systems. Our analysis explored the influence of the number of taps on the filter performance, filter tunability, and the precision required of tap weight to maintain the desired filter performance.

To understand the requirement on the number of taps for a given filter bandwidth we used a simple filter design algorithm based on spectrum sampling. The use of window functions greatly reduced the side lobe levels for a given number of taps. In Figure 5-3 we show that the Blackman, Kaiser, and Chebyshev windows can provide the type of side lobe suppression needed for the stringent filtering requirements presented in the previous section. We calculated filter pass-bandwidth (for a fixed input bandwidth) as a function of the number of taps and not surprisingly, we find the bandwidth is inversely proportional to the number of taps. This is illustrated in Figure 5-4.
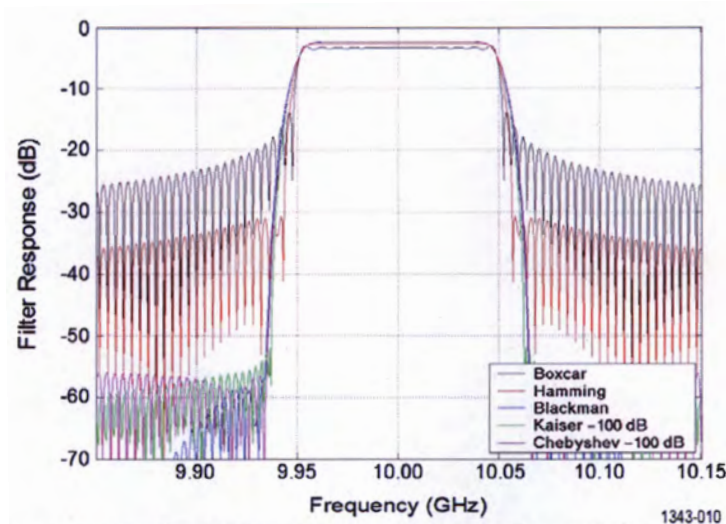

Figure 5-3 | FIR filter response using various window functions. Proper choice of window function provides dramatic improvement in out-of-band rejection.
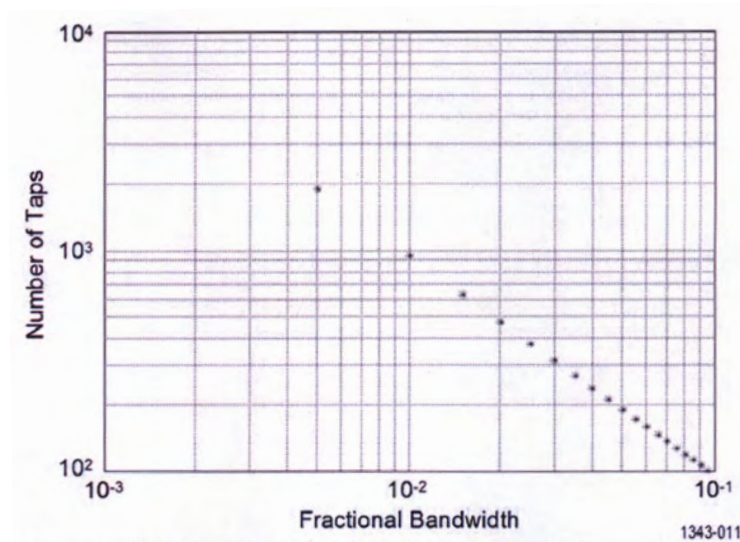
Figure 5-4 | Number of taps vs. FIR filter fractional BW. Tap count scales inversely with filter bandwidth.

For example, given an input bandwidth of 10 GHz, a filter pass-bandwidth of 1 GHz requires a filter order of about 100 while a 100 MHz bandwidth requires a filter order of about 1,000 and so on.

Another consideration is the tunability of the filter. Although the physical mechanism for tuning the filter may allow fast tuning, the tap weight computational algorithm must also be fast enough to support adequate frequency tuning agility. If the tap weights must be recalculated for each tuning step, then the algorithm will severely limit the tuning speed of the filter. Fortunately the frequency shifting property allows for simple modification of the tap weights and tuning of the filter. Once a filter has been designed to meet the requirements of an equivalent base band (i.e. low pass) filter, a simple cosine weighting function given by $w[i] = \cos(f_c/f_{max}i)$, can be used to shift the spectral pass band to the desired center frequency. To demonstrate this, a filter was designed by a Kaiser window method to have a pass-band width of 100 MHz. Then the tap weights were scaled with the weighting function for several values of f_c. The plot of the resulting filter spectra is shown in Figure 5-5.
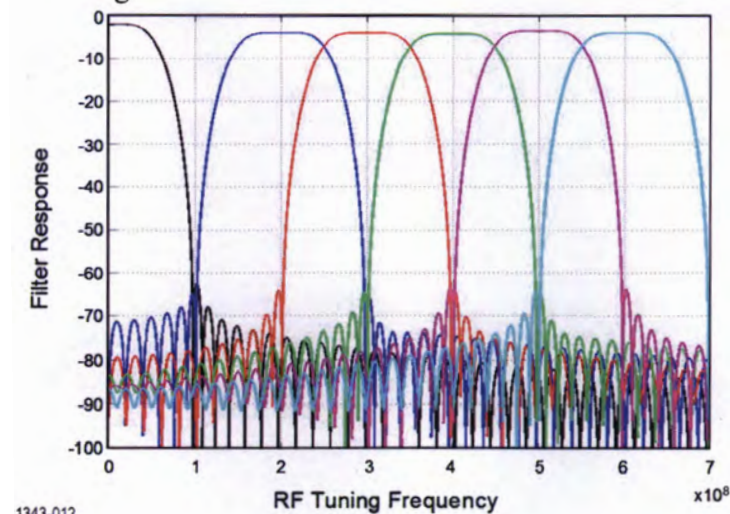

1343-012

27

Figure 5-5 | Frequency tuning of transversal filter. Filter center frequency can be shifted using a computationally simple weighting function.

Finally we investigated the required precision of the tap weight values. A random number uniformly distributed between the negative and positive precision value was added to the ideal tap weight values for examination of the required precision. The precision was specified as the number of bits relative to the maximum tap weight value (e.g. n-bits of precision $\equiv 1/2^n$ x ideal value). In Figure 5-6 we plot key filter performance metrics vs. the number of bits of precision.
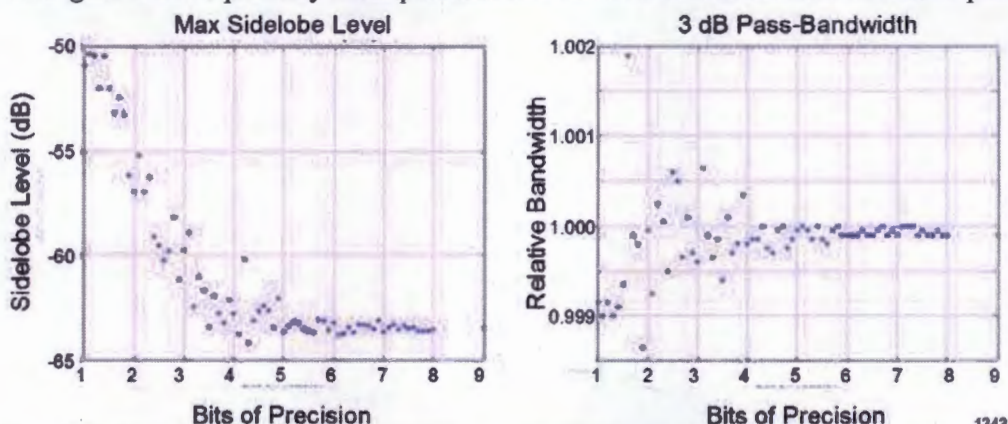

Figure 5-6 | FIR transversal filter performance vs. tap weight precision. Key performance metrics suffer negligible degradation for 5 bits (~3%) random variation from ideal tap weights.

Non-integer bits are also included to more clearly identify the trend in the plots. Also for comparison, the ideal filter performance is shown on the graph as 9 bits of precision.

It should also be noted that the data presented represent a single "sample-run" of the additive random variation and not a statistical average or worst case. Nevertheless, the results indicate that about 5 bits of precision are adequate to maintain the required loss, sidelobe level, and pass bandwidth. With 6 bits of precision, there is little variation from the ideal case.

In conclusion, a photonically implemented FIR filter with a 50 MHz passband and 60 dB of channel-to-channel isolation requires about 2000 taps. For a 10 GHz filter bandwidth the filter FSR = 20 GHz and the ideal tap spacing is 15 mm. If we assume 5 bit precision on the tap spacing the resulting positional accuracy is about ± 0.5 mm, which is equivalent to a delay accuracy in the waveguide of 1.7 ps. This is a somewhat more stringent requirement than presented in the proposed program goals.

5.4.2 Photonic filter RF performance - noise figure and SFDR

The RF performance of the photonic delay-line processor will obviously be application dependent, and must be evaluated in the context of the specific signal processing function under implementation. In the case of our proposed demonstration processor, we consider the performance of an iPhoD circuit configured as a transversal filter. Within the RF passband, this filter resembles a simple point-to point fiber link and it is within this band that standard RF performance criteria such as noise figure and spur-free dynamic range are most meaningful.

We analyze a simple intensity-modulated link implementation of a transversal filter and then extend the analysis to a balanced detection configuration to illustrate the benefits that it provides. In brief, we find that the simple link places severe requirements on laser RIN in order to achieve low noise figure and high dynamic range. By using balanced detection we cancel the RIN by at least 30 dB, reducing the laser RIN requirement to acceptable levels.

Consider a photonic transversal filter configured as a bandpass filter with passband □f and insertion loss I.L. Note that I.L. is the in-band loss for a particular filter design exclusive of optical losses. First we consider the link representation of the simple photonic filter shown in Figure 5-7.
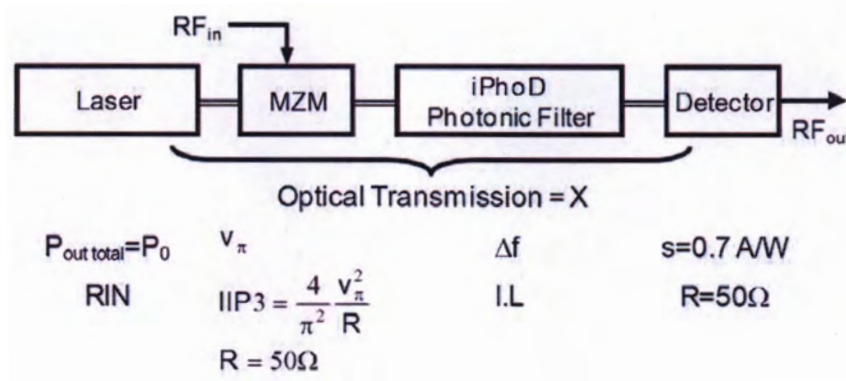

Figure 5-7 | Photonic transversal filter - RF model. Filter RF performance is based on I-M link.

Most of the symbols are self-explanatory. X is the aggregate optical loss through the optical circuit and s is the detector responsitivity.

For an input signal, $v_0 \cos(\omega t)$, the output photocurrent is

$$i_p = \tfrac{1}{2}P_0 sX - \tfrac{1}{2}P_0 sX(\text{I.L.})^{\frac{1}{2}} \frac{\pi}{2v_\pi} v_0 \cos(\omega t) + \text{distortion terms} + \text{noise}$$

$$(5\text{-}1)$$

The dominant contributor to distortion terms in the filter output is the nonlinear transfer function of the modulator, which is the well-known raised cosine curve, which owing to its symmetry at the quad-bias point, produces no even order products. The relevant terms then are the two-tone, third order mixing products. Fourier analysis of a MZM biased at its quadrature point yields the following relationship between the modulator's characteristic voltage, v_π, and the link input IP3 (IIP3).

$$\text{IIP3} = \frac{4}{\pi^2} \frac{v_\pi^2}{R}$$

$$(5\text{-}2)$$

We can express the spur-free dynamic range in terms of the link noise figure, F, and the IIP3 as follows,

$$\text{SFDR} = \left(\frac{\text{IIP3}}{F\,kT}\right)^{2/3} \Rightarrow \tfrac{2}{3}\left(\text{IIP3} - F - kT\right) \quad \text{in units of dB Hz}^{2/3}$$

$$(5\text{-}3)$$

We define the link RF gain as

$$G \equiv \frac{P_{out}}{P_{in}} = \frac{\left[\frac{1}{2}P_0sX(I.L.)^{\frac{1}{2}}\frac{\pi}{2v_\pi}v_0\right]^2}{v_0^2}R^2 = \left[\frac{\pi P_0sXR}{4v_\pi}\right]^2(I.L.)$$

(5-4)

The output noise PSD is due to detector thermal noise, input thermal noise, shot noise on the DC photocurrent, and laser RIN so we have (where q is the electronic charge)

$$P_N = kT + GkT + P_0sTqR + 10^{\frac{RIN}{10}}\left(\frac{1}{2}P_0sT\right)^2 R\ I.L.$$

(5-5)

The noise figure is given by the ratio of the equivalent input noise to thermal noise

$$F = \frac{EIN}{kT} = \frac{P_N/G}{kT} = \frac{1}{G}+1+\frac{P_0sXqR}{GkT}+\frac{10^{\frac{RIN}{10}}\left(\frac{1}{2}P_0sX\right)^2 R\ I.L.}{GkT}$$

(5-6)

Assume the following parameter values: s = 0.7 A/W; X = -6dB = 0.25; I.L. = -4 dB = 0.4; and R = 50□. Also a typical value of v_π for commercially available modulators is 5 volts. Substitution of Eq. (5-4) into Eq. (5-6) with these parameter values gives

$$F = \frac{0.89}{P_0^2}+1+\frac{375}{P_0}+4.97*10^{19}*10^{\frac{RIN}{10}}$$

(5-7)

Now let's consider a filter with requirements of 60dB dynamic range and a filter passband of 50 MHz. For a 5 volt modulator Eq. (5-2) gives an IIP3 of 0.637 W or +23 dBm. Using standard SFDR algebra we find the noise figure required of the link.

$$F(dB) = IIP3 - \tfrac{3}{2}SFDR - kT - 10\log(BW) = 28 - 90 + 174 - 77 = 30dB$$

(5-8)

As an example, let's assume that P_0 = 0.5 W and then calculate the RIN value required to achieve a 30 dB noise figure. We find that the laser RIN must be better than -172 dBc/Hz. This is a very difficult value to achieve, which motivated us to employ the balanced detection architecture, shown in Figure 5-8, to mitigate the effect of laser RIN.
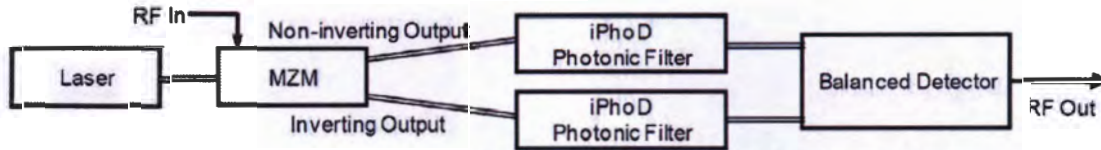

Figure 5-8 | Link model of photonic transversal filter. A balanced detection architecture mitigates RIN and enhances the filter's SFDR performance.

In this architecture we use a dual output MZM and a pair of identical photonic filters. Thus at the upper filter's optical outputs we have RIN + P_{signal}, and at the lower filter's outputs we have RIN - P_{signal}. We use a balanced photodetector to differentially detect the two filter outputs to arrive at the output signal, $2P_{signal}$ + (residual RIN).

A typical value for common-mode rejection for commercially available balanced detectors is 30 dB, ·which equates to a 30 dB reduction of the RIN. As described in the following section, we have measured greater than 40 dB of common-mode rejection in our single-string photonic link testbed

5.5 Initial processor circuit analysis

Our baseline demonstration processor is a microwave photonic transversal filter. The concept is shown in Figure 5-9.
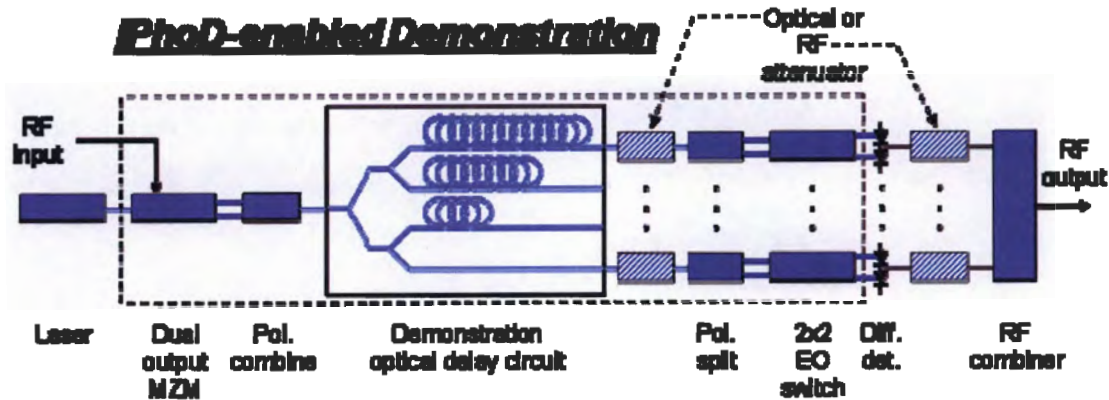

Figure 5-9 | iPhoD System Applications: RF Filter Detail.

5.5.1 Single-string demonstration testbed

Key RF system requirements that will impact a photonic filter approach include power consumption and linearity. These will be driven by the standard characteristics of the photonic link within the filter. We constructed the single-string demonstration circuit shown schematically in Figure 5-10 in order to verify our link design and characterize the peripheral components that will eventually be combined with the iPhoD waveguides to construct the demonstration processor in Phase III.
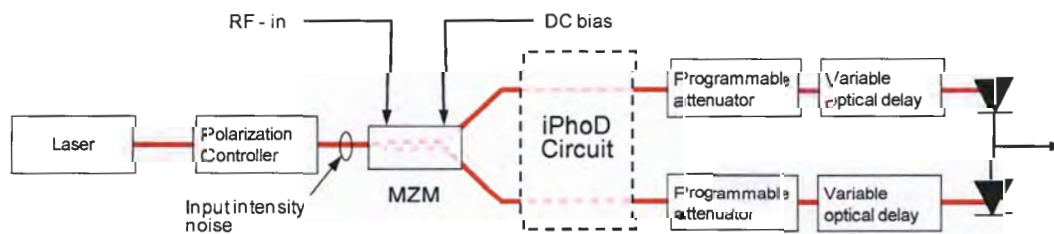

Figure 5-10 | Single-String Demonstration Testbed.

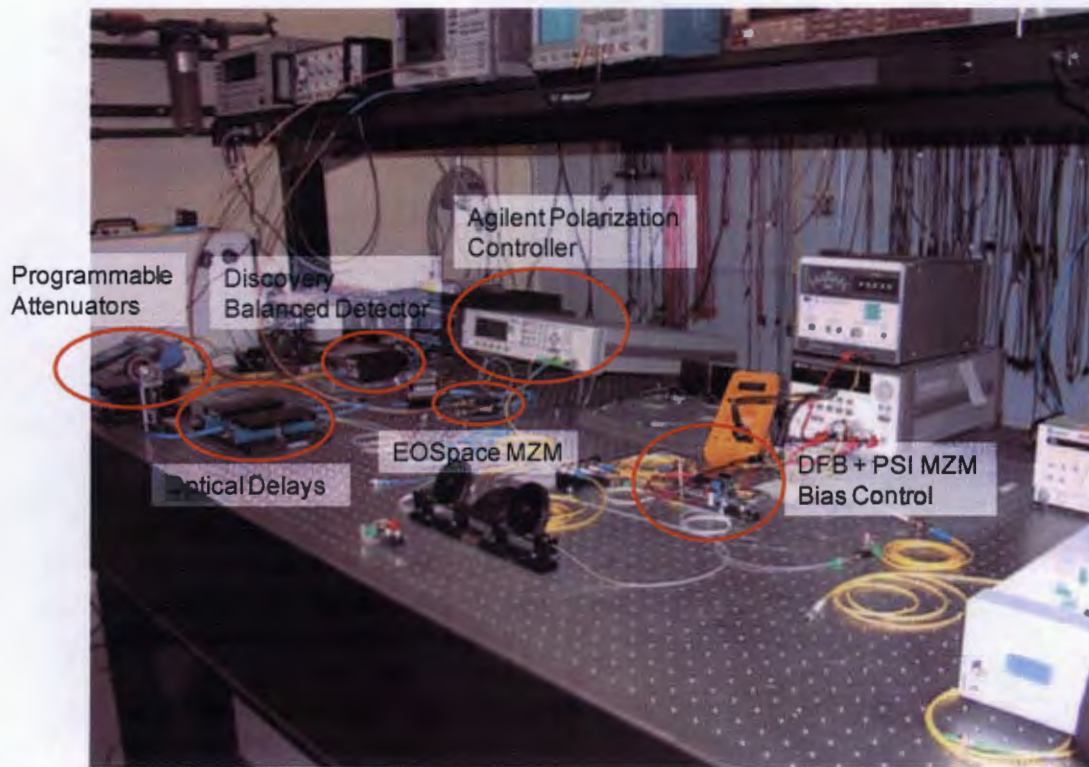Figure 5-11 is a photograph of our link setup showing the key components.

Figure 5-11 | Single-String Testbed Layout.

We have measured the following basic link characteristics at a signal frequency of 2 GHz.
Common mode rejection: 43 dB
- Far surpasses the typical reported values of 20 to 25 dB

Link Gain: -31.7 dB
- ~1.8 dB less than expected based on vendor's stated v_π

Input IP3T: 19.9 dBm
- ~2.2 dB greater than expected based on vendor's stated v_π

Input IP2H: > 66 dBm
- Indicates very good MZM bias control

Link SFDR: 105 dB $Hz^{2/3}$
- Shot noise limited (0.45 mA / detector)

The discrepancy between measured and calculated values for the link gain and IIP3 indicate that the effective v_π of our modulator is about 20% greater than the specified value.

5.5.2   Single string testbed linearity enhancement

We investigated a technique for improving the link linearity. We modified our testbed as shown in Figure 5-12 and performed an experiment similar to that done previously by Johnson and Roussell [19] who used a dual polarization technique that cancels the cubic dependence of the 3rd order intermodulation terms (IM3s).
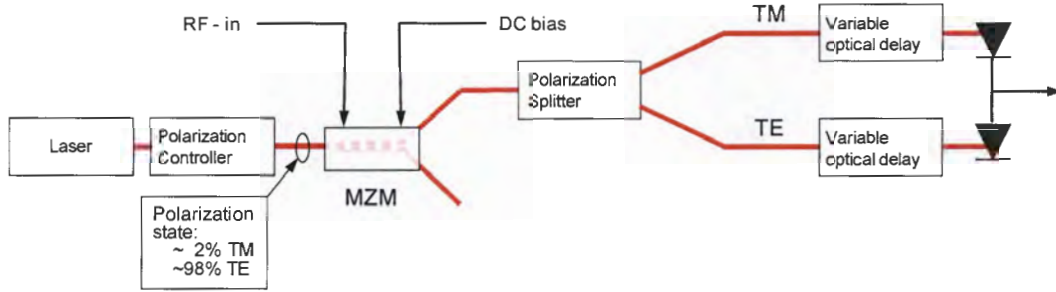
Figure 5-12 | RF Testbed setup for linearization of the MZM modulator.

In this experiment we consider a MZM with two different modulation sensitivities, i.e. different values for v_π, which is the case for $LiNbO_3$ where the TM polarization sees the EO coefficient r_{33} and the TE polarization sees the EO coefficient r_{13}. Define $vr = v_{\pi TE} / v_{\pi TM}$. (We measured vr for our $LiNbO_3$ modulator.) We can then adjust the optical power for the TE and TM modes of the modulator such that their cubic contributions to IM3 cancel. In order to cancel the cubic terms $P_{optical}{}^{TE} = 1/\square^{\square} P_{optical}{}^{TM}$. The total IM3 is significantly reduced but will still be present with a ($P_{RF}{}^5$ + higher order) dependence. This process is illustrated in Figure 5-13.
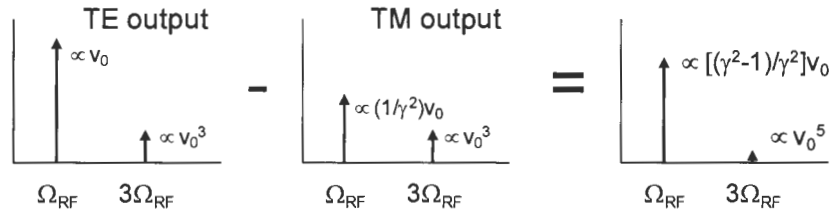

Figure 5-13 | Spurious signal cancellation using polarization multiplexing.

Using this technique we have measured a 25 dB reduction in spurious signal power. The result of this is that the link SFDR is improved by $1/3 * 25 = \sim 8$ dB for a given amount of optical power, which is the most significant driver for RF photonic systems.

We used an EOspace MZM, for which we measured the following values of v_π for the two orthogonal input polarization states:

$$TE - v_\square{}^{TM} = 5.2 \ V$$
$$TE - v_\square{}^{TE} = 20.6 \ V$$

Our analysis showed that for the purpose of calculating link gain and noise figure the linearized link exhibits a v_π slightly larger than the TE value, producing a slight reduction in gain. Also, under an ideally matched condition where the cubic contributions from the TE and TM polarizations cancel exactly we would expect the spurious signal to exhibit a $P_{RF}{}^5$ dependence. Figure 5-14 shows our data for the TE-only link and the TE-TM (linearized) link.
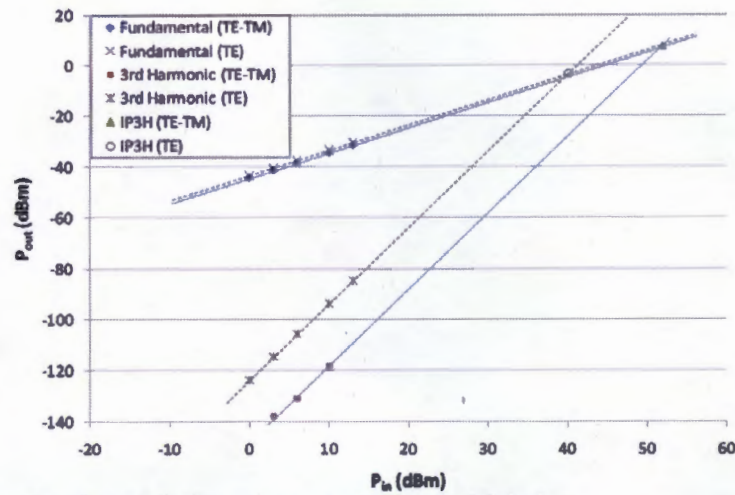
Figure 5-14 | Spurious signal cancellation using polarization multiplexing.

We see that our data for the link gain behaves as expected and that the spurious 3rd harmonic is suppressed significantly. We observed > 12 dB increase in the IP3H.

However the spurs follow a P_{RF}^3 dependence. It turns out that this is due to a slight deviation from the ideal optical power ratio for the TE and TM components resulting in incomplete cancellation of their cubic contributions. This is illustrated in Figure 5-15 where we compare our data with analytical results. The dashed linearized 3H line in the figure is for the situation where we have ideal cancellation and exhibits a slope of 5. The solid linearized 3H line is calculated for the case of ~25 dB cancellation of the cubic contributions and exhibits a slope of 3 at the power levels we measured. At higher input powers its slope increases to match the ideal curve, then both curves roll off with a continuing increase in input power. We see that we could expect to obtain even greater reduction in spurious signals by improving our cancellation ratio.
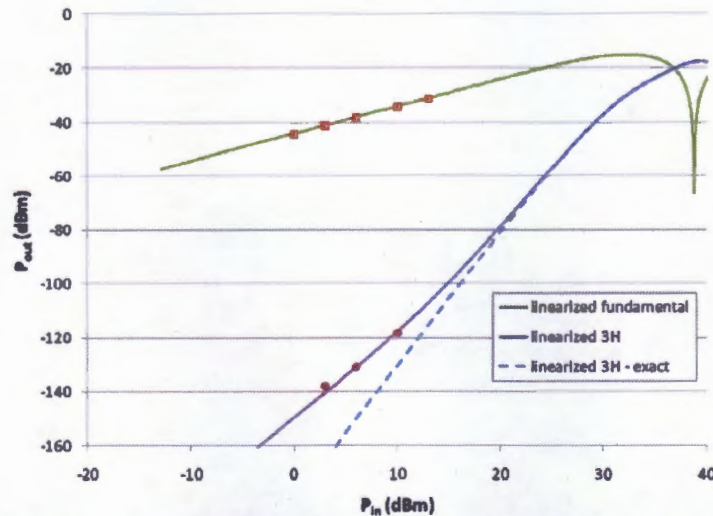

Figure 5-15 | Comparison of experimental data with analytical results. The data indicates a cancellation ratio of 25 dB was achieved in the experiment.

5.6 Summary

The *Ultra-low Loss, Chip-Based Hollow-Core Waveguide Using High-Contrast Grating* program under the DARPA iPhoD program has produced a sound technical foundation for future optical delay-based processors and set the stage for the development of the critical elements of an all-optical signal processing architecture for a variety of military missions.

NGAS's iPhoD program's experimental work has demonstrated much of the basic performance capability for delay-based system architectures and enabled us to identify technical issues that should be addressed as this technology matures.

6. Future Plans

Although the loss of both types of HCW has already been very low, there is still a large room for improvements. For the first type, as is seen in Fig. 3-2, the HCG designs do not hit on the lowest region on the parameters space. Through further optimization, much lower loss is expected. For the larger core HCW, the Si/Air DBR can be replaced by Si/SiO$_2$ DBR, which can provide a full photonic bandgap and high reflection for all incident angles of lights [13]. In this case, much aggressive bending and propagation length can be achieved with low loss.

To further address the bending issues, another type of HCW is proposed. This is another truly novel structure. Instead of the in-plane HCGs as shown in Fig. 3-1, the HCG can be rotated 90° as posts, shown in Fig. 6-1. The light would thus be confined lateral by the HCG posts. In the vertical direction, light can be confined in the center region through effective index method by choosing different materials for the center and the two ends of the posts. This defines the core and cladding vertically; although their HCG parameters are the same, the different refractive index of the material can induce different effective indices. This vertical HCG-HCW has advantages over the in-plane HCG-HCW in terms of bending loss. In the previous case demonstrated in Section 3, the in-plane confinement is provided by effective index method, which can be modeled as total internal reflection. This limits the radius of curvature of the in-plane bending into a large value. The vertical HCG-HCW, on the other hand, offers the in-plane confinement by HCGs, which can be designed and optimized to support high reflection over a large range of incident angles. This would thus lessen the stringent limits of in-plane bending, such that the bending radius of curvature can be small. As a preliminary simulation result, Fig. 6-1b shows the mode profile of a vertical HCG-HCW after 300 μm propagation in finite-difference time-domain method (FDTD) simulation. The core region is 3 μm thick (Al$_{0.1}$Ga)InAs lattice matched to the 4 μm InP cladding region on each side. The waveguide width is 4 μm. The period, bar width, and thickness of the HCG is optimized to be 675 nm, 285 nm and 400 nm respectively. This simulation verifies the effective index method, and fabrication is currently undergoing.
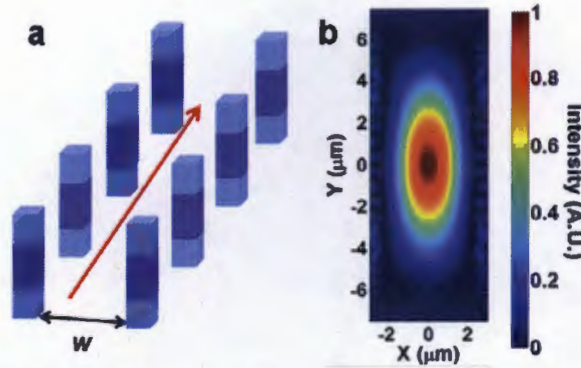
Figure 6-1 | Vertical HCG-HCW. a, Schematic of the proposed vertical HCG-HCW. The arrays of HCG posts form the HCW with width w. Each HCG post is composed of three sections vertically: high refractive index material for the center region functions as core, and low refractive index material for the two end region functions as cladding. Vertical confinement is through effective index method. **b**, Mode profile of the vertical HCG-HCW simulated by finite-difference time-domain method (FDTD). The propagation length is 300 μm. The core region is 3 μm thick (Al0.1Ga)InAs lattice matched to the 4 μm InP cladding region on each side. The waveguide width is 4 μm. The period, bar width, and thickness of the HCG is optimized to be 675 nm, 285 nm and 400 nm respectively.

Applications of HCW, in particular, on-chip gas sensors and low-energy all-optical switches, would be explored. The sidewall-free HCG-HCW allows the gas to penetrate instantly, and thus provides a very fast response time. Low-energy all-optical switches utilize the resonance effect of HCG. Two vertical HCG-HCWs are placed in parallel, and separated by a shared HCG post array. By shining external light into this shared array, the refractive index of the material changes and the HCG falls into the resonance condition and becomes "transparent". Light can thus switch from one channel to another. This effect is illustrated in Fig. 6-2. The resonance of the HCG can be designed to be very sharp, and thus the switching energy can be extremely small.
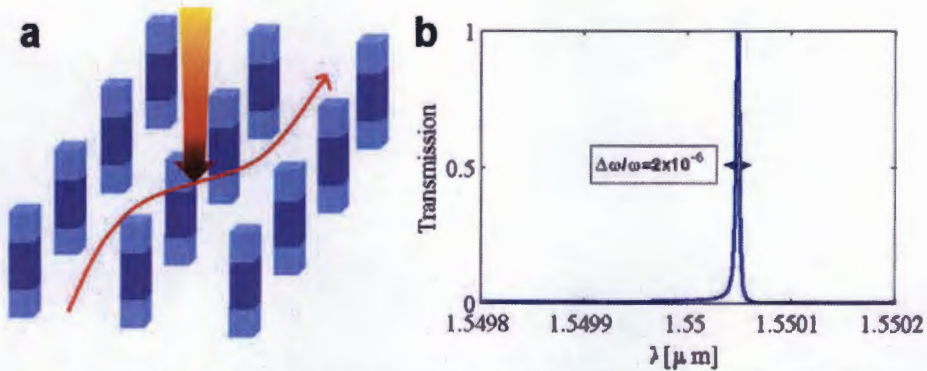
Figure 6-2 | Low energy all optical switch. a, Two vertical HCG-HCWs are placed in parallel with a single array of HCG posts as separation. The HCG is designed such that it operates closed to the resonance condition. When external light is shined onto this array, the HCG falls into resonance and becomes "transparent". Light can thus switch from one waveguide to the adjacent one. **b**, A narrow band HCG resonance.

Other future plans include the system level realization of photonic transverse filter and the processor circuit.

7. Broader Impact

The UC Berkeley iPhod project has not only developed the novel HCG-HCWs, but also created a much broader impact. It has built up an HCG based Si photonic platform. Hollow-core waveguide, vertical coupler [20], planar dielectric lens [21], optical switches, optical buffers [22] etc. can be seamless integrated into this platform. Heterogeneous integration of HCG-VCSEL is also feasible. Various fabrication processes are developed, such as high resolution DUV lithography, high aspect ratio deep etch, substrate removal, and wafer bonding. System level studies are conducted to advance the photonic circuit and processor design and architecture. All these technologies will fit into other ongoing DARPA programs such as "short-range, wide field-of view extremely agile, electronically steered photonic emitter (SWEEPER)", as well as the future programs such as "electronic-photonic heterogeneous integration (E-PHI)".

8. Project Summary

HCG based HCWs are developed and experimentally demonstrated in iPhod project. The following lists what we have achieved through the project:
- HCG-HCW with novel lateral confinement scheme. 0.37 dB/cm propagation loss is achieved for a waveguide height d~9 μm.
- Large core HCG-HCW with DBR structure for lateral confinement. <0.1 dB/m propagation loss is estimated based on the loss measurement.
- Long waveguide length with spiral layout or folded layout in 6'' wafer.
- Preliminary results on nonlinearity measurement. The results is limited by our launching light power, OSA noise floor and waveguide length.
- Process development of Si photonics, including high resolution DUV lithography, high aspect ratio dry etching, substrate removal, wafer bonding and SOI wafer warp correction.
- Development of HCG based photonic platform.
- Analysis of chromatic dispersion and nonlinearity variation of HCG-HCW, and its effect on high-speed digital and analog signals and systems.
- Analysis of the application of HCG-HCW in matched filter.
- Analysis of the application of HCG-HCW in the future optical delay-based processors and critical elements of an all-optical signal processing architecture for a variety of military missions.
- Develop a processor architecture that supports the results of applications study of HCG-HCW.
- Quantify compatibility of architecture approaches with HCG waveguide technology.

Future plan:
- Low loss on long waveguide length with turning or curving.
- Vertical HCG-HCW to achieve low loss for a long waveguide length with turning or curving.
- Si/SiO$_2$ DBR structure as lateral confinement scheme to achieve low loss for a long waveguide length with turning or curving.
- Gas sensing application development.
- Low-energy all-optical switches based on vertical HCG-HCW.
- System level realization of photonic transverse filter and the processor circuit.

Broader impact:

- Establishing of an HCG-based Si photonic platform and related processes.
- Technologies transferring to other DARPA projects such as SWEEPER and E-PHI.

The following chart compares the Phase I goal, proposed tasks and the UCB team result.

	Phase I Goal	UCB Result
Waveguide Loss (dB/m)	**0.1**	**0.1**
Time Delay (ns)	**100**	**3.3**
Power Handling (mW)	**20**	**>65**
Footprint (cm^2)	**50**	**~0.5 for 3.3ns time delay**
Optical wavelength	**1.55 μm**	**1.55 μm**
Polarization	**Linear**	**Linear**

Phase I Timeline	Original Proposed Plan	Result
6th Month	• Develop an analytical model for 2D HCG-HW	Finished
	• Conceptual design of 2D HCG-HW	Finished
	• FDTD/FEM simulations of 1D HCG-HW and comparison against analytical formulation	Finished
	• Develop nanofabrication process and wafer bonding for 2D HCG-HW	Finished
12th Month	• FDTD/FEM simulation of 2D HCG-HW and comparison against analytical formulation	Finished
	• Fabricate 2D HCG-HW	Finished
	• Measure optical loss, optical phase, spectral width, power handling	Finished
	• Develop an analytical model for spiral WG, 90- and 180-degree bends	Finished
	• Develop well-characterized benchmark systems that facilitate an unambiguous quantitative comparison between theory and experiment	Finished
	• Applications study complete	Finished
18th Month	• Use comparisons between experimental results and simulation to optimize 2D HCG-HW	Finished
	• Measure optical loss, optical phase, spectral width, power handling	Finished

	Status
• Fabricate 2D HCG-HW rings or meanders to achieve 100 ns delay	In Progress
• Determine and characterize the sensor sensitivity	In Progress
• Determine and characterize the RF filter response	In Progress
• Determine and characterize the bit rate and packet length for the packet switching application	In Progress
• Architecture study complete	Finished
• Initial design recommendation	Finished

9. Publications by iPHOD Team

1) Weijian Yang, James Ferrara, Karen Grutter, Anthony Yeh, Christopher Chase, Vadim Karagodsky, Yang Yue, Alan E. Willner, Ming C. Wu and Connie J. Chang-Hasnain, "Low-Loss Hollow-Core Waveguide on a Silicon Substrate", manuscript under preparation.

2) Alan E. Willner, Yang Yue, Hao Huang, and Lin Zhang, "Signal Propagation Effects in HCG Hollow-Core Waveguides," Invited Paper, *Society of Photo-Instrumentation Engineers (SPIE) Photonics West*, Conference 8270, paper 8270-15, Jan. 2012, San Jose, CA.

3) Connie J. Chang-Hasnain, "**High-contrast grating optoelectronics**", Invited Paper, *Society of Photo-Instrumentation Engineers (SPIE) Photonics West*, Conference 8270, paper 8270-01, Jan. 2012, San Jose, CA.

4) James Ferrara, Weijian Yang, Anthony Yeh, Karen Grutter, Christopher Chase, Vadim Karagodsky, Devang Parekh, Yang Yue, Alan E. Willner, Ming C. Wu, and Connie J. Chang-Hasnain, "Low-loss Hollow-core Waveguide Using High-contrast Sub-wavelength Grating," *Society of Photo-Instrumentation Engineers (SPIE) Photonics West*, Conference 8270, paper 8270-17, Jan. 2012, San Jose, CA.

5) Hao Huang, Yang Yue, Lin Zhang, Bishara Shamee, Christopher Chase, Forrest G. Sedgwick, Moshe Tur, Connie J. Chang-Hasnain, and Alan E. Willner, "Tapped Delay-line Matched Filtering using a High-Contrast Grating Hollow-Core Waveguide," *IEEE Photonics Society Annual Meeting*, paper MS2, Arlington, VA, Nov. (IEEE, Piscataway, NJ, 2011).

6) Weijian Yang, James Ferrara, Karen Grutter, Anthony Yeh, Christopher Chase, Vadim Karagodsky, Devang Parekh, Yang Yue, Alan E. Willner, Ming Wu, and Connie J. Chang-Hasnain, "Novel Three-dimensional Hollow-core Waveguide Using High-contrast Sub-wavelength Grating," *Conference on Lasers and Electro-Optics(CLEO)*, paper CThHH4, Baltimore, MD, May 2011 (Optical Society of America, Washington, D.C., 2011).

7) YangYue, Lin Zhang, Xue Wang, Hao Huang, Weijian Yang, James Ferrara, Vadim Karagodsky, Christopher Chase, Moshe Tur, Connie J. Chang-Hasnain, and Alan E. Willner, "Hollow-Core-Waveguides using Adiabatically Chirped High-Contrast-Gratings for a >10× Loss Reduction," *Conference on Lasers and Electro-Optics(CLEO)*, paper CThZ4, Baltimore, MD, May 2011 (Optical Society of America, Washington, D.C., 2011).

8) Xue Wang, Yang Yue, Lin Zhang, Hao Huang, Yan Yan, Weijian Yang, James Ferrara, Vadim Karagodsky, Christopher Chase, Moshe Tur, Connie J. Chang-Hasnain, and Alan E. Willner, "Tunable Optical Coupling in a Low-Loss Hollow Core Waveguide Using Adiabatically Chirped High-Contrast-Gratings and MEMS Actuators," *Conference on Lasers and Electro-Optics (CLEO)*, paper JTuI74, Baltimore, MD, May 2011(Optical Society of America, Washington, D.C., 2011).

9) Bishara Shamee, Lin Zhang, Yang Yue, Hao Huang, Xue Wang, Moshe Tur, Alan E. Willner, Chris Chase, Vadim Karagodsky, Forrest Sedgwick, and Connie J. Chang-Hasnain, "FIR

Analog Filter Dependence of HCG-Based Hollow-Core Waveguides upon Varying of Waveguide Parameters," *Conference on Lasers and Electro-Optics(CLEO)*, paper JWA124, Baltimore, MD, May 2011 (Optical Society of America, Washington, D.C., 2011).

10) Hao Huang, Yang Yue, Lin Zhang, Xue Wang, Christopher Chase, Devang Parekh, Forrest Sedgwick, Moshe Tur, Ming Wu, Connie Chang-Hasnain, and Alan E. Willner, "Analog Signal Performance of a Hollow-Core-Waveguide using High-Contrast-Gratings," IEEE/OSA *Conference on Optical Fiber Communications (OFC)*, paper OThA3, Los Angeles, CA, Mar. 2011 (Optical Society of America, Washington, D.C., 2011).

11) YangYue, Lin Zhang, Forrest G. Sedgwick, Bishara Shamee, Weijian Yang, James Ferrara, Christopher Chase, Raymond G. Beausoleil, Connie J. Chang-Hasnain, and Alan E. Willner, "Chromatic Dispersion Variation and Its Effect on High-Speed Data Signals due to Structural Parameter Changes in a High-Contrast-Grating Waveguide," *IEEE Photonics Society Annual Meeting*, paper ThB2,Denver, CO, Nov. (IEEE, Piscataway, NJ, 2010).

12) Yang Yue, Lin Zhang, Jian Wang, Yinying Xiao-Li, Bishara Shamee, Vadim Karagodsky, Forrest G. Sedgwick, Werner Hofmann, Raymond G. Beausoleil, Connie J. Chang-Hasnain, and Alan E. Willner, "A "Linear" High-Contrast Gratings Hollow-Core Waveguide and its System Level Performance," *IEEE/OSA Conference on Optical Fiber Communications (OFC)*, paper OTuI5, San Diego, CA, Mar. 2010 (Optical Society of America, Washington, D.C., 2010).

10. Reference

1. Miura, T., Koyama, F. & Matsutani, A. Modeling and fabrication of hollow optical waveguide for photonic integrated circuits. *Jpn. J. Appl. Phys.* **41**, 4785-4789 (2002).
2. Miura, T. & Koyama, F. Low-loss and polarization-insensitive semiconductor hollow waveguide with GaAs/AlAs multi-layer mirrors. *Jpn. J. Appl. Phys.* **43**, L21-L23 (2004).
3. Zhou, Y., Karagodsky, V., Pesala, B., Sedgwick, F. G. & Chang-Hasnain, C. J. A novel ultra-low loss hollow-core waveguide using subwavelength high-contrast gratings. *Opt. Express* **17**, 1508-1517 (2009).
4. Mateus, C. F. R., Huang, M. C. Y., Chen, L., Chang-Hasnain, C. J. & Suzuki, Y. Broad-band mirror (1.12–1.62 μm) using a subwavelength grating. *IEEE Photon. Technol. Lett.*, **16**, 1676–1678 (2004).
5. Huang, M. C. Y., Zhou, Y. & Chang-Hasnain, C. J. A surface-emitting laser incorporating a high-index-contrast subwavelength grating. *Nature Photon.*, **1**, 119–122 (2007).
6. Chang-Hasnain, C. J., Zhou, Y., Huang, M. C. Y. & Chase, C. High-contrast grating VCSELs. *IEEE J. Sel. Topics Quantum Electron.*, **15**, 869-878 (2009).
7. Chase, C., Rao, Y., Hofmann, W. & Chang-Hasnain, C. J. 1550nm high contrast grating VCSEL. *Opt. Express* **18**, 15461-15466 (2010).
8. Karagodsky, V., Pesala, B., Sedgwick, F. G. & Chang-Hasnain, C. J. Dispersion properties of high-contrast grating hollow-core waveguides. *Opt. Lett.* **35**, 4099-4101 (2010).
9. Knox, R. M. & Toulios, P. P. Integrated circuit for the millimeter through optical frequency range. *Proc. Symp. Submillimeter Wave*, J. Fox and M. H. Schlam, eds. Polytechnic Institute of Brooklyn, 497-516 (1970).
10. Pesala, B., Karagodsky, V., Koyama, F. & Chang-Hasnain, C. J. Novel 2D high-contrast grating hollow-core waveguide. *Proc. Conf. on Lasers and Electro-Optics,* Optical Society of America (2009).

11. Hu, J. *et al.* Low-loss high-index-contrast planar waveguides with graded-index cladding layers. *Opt. Express* **15**, 14566-14572 (2007).
12. Moharam, M. G. & Gaylord, T. K. Rigorous coupled-wave analysis of planar-grating diffraction. *J. Opt. Soc. Amer.*, **71,** 811–818 (1981).
13. Fink, Y., *et al.* A dielectric omnidirectional reflector. *Science*, **282**, 1679-1682 (1998).
14. Yue, Y., *et al.* Chromatic dispersion variation and its effect on high-speed data signals due to structural parameter changes in a high-contrast-grating waveguide. *Proc. IEEE Photonics Society Annual Meeting,* Institute of Electrical and Electronics Engineers (2010).
15. Yue, Y., *et al.* A "linear" high-contrast gratings hollow-core waveguide and its system level performance. *Proc. Conference on Optical Fiber Communications,* Optical Society of America (2010).
16. Huang H., *et al.*, Analog signal performance of a hollow-core-waveguide using high-contrast-gratings. *Proc. Conference on Optical Fiber Communications,* Optical Society of America (2011).
17. Shamee, B., *et al.*, FIR analog filter dependence of HCG-based hollow-core waveguides upon varying of waveguide parameters. *Proc. Conf. on Lasers and Electro-Optics,* Optical Society of America (2011).
18. Huang H., *et al.*, Tapped delay-line matched filtering using a high-contrast grating hollow-core Waveguide. *Proc. IEEE Photonics Society Annual Meeting,* Institute of Electrical and Electronics Engineers (2011).
19. Johnson, L.M. & Roussell, H.V. Reduction of intermodulation distortion in interferometric optical modulators. *Opt. Lett.* **13**, 928-930 (1988).
20. Zhu, L. Karagodsky, V., Yang, W. & Chang-Hasnain, C. J. Novel high efficiency vertical optical coupler using subwavelength high contrast grating. *Proc. Conf. on Lasers and Electro-Optics,* Optical Society of America (2011).
21. Lu, F., Sedgwick, F. G., Karagodsky, V., Chase, C. & Chang-Hasnain, C. J. Planar high-numerical-aperture low-loss focusing reflectors and lenses using subwavelength high contrast gratings. *Opt. Express* **18**, 12606-12614 (2010).
22. Sun, T., Sedgwick, F. G., Yang, W., Karagodsky, V. & Chang-Hasnain, C. J. Low-loss slow light in high contrast grating hollow waveguides. *Proc. Conf. on Lasers and Electro-Optics,* Optical Society of America (2011)